Ultramafic clasts from the South Chamorro serpentine mud volcano reveal a polyphase serpentinization history of the Mariana forearc mantle

Wolf-Achim Kahl[a,*], Niels Jöns[a,b], Wolfgang Bach[a], Frieder Klein[c], Jeffrey C. Alt[d]

[a] Department of Geosciences, University of Bremen, Klagenfurter Straße (GEO), D-28359 Bremen, Germany

[b] Institut für Geologie, Mineralogie und Geophysik, Ruhr Universität Bochum, D-44780 Bochum, Germany

[c] Department of Marine Chemistry and Geochemistry, Woods Hole Oceanographic Institution, Woods Hole, MA, 02543, USA

[d] Dept. Earth and Environmental Sciences, The University of Michigan, Ann Arbor, MI 48109 USA

*Corresponding author: E-mail address: wakahl@uni-bremen.de

ABSTRACT

Serpentine seamounts located on the outer half of the pervasively fractured Mariana forearc provide an excellent window into the forearc devolatilization processes, which can strongly influence the cycling of volatiles and trace elements in subduction zones. Serpentinized ultramafic clasts recovered from an active mud volcano in the Mariana forearc reveal microstructures, mineral assemblages and compositions that are indicative of a complex polyphase alteration history. Petrologic phase relations and oxygen isotopes suggest that ultramafic clasts were serpentinized at temperatures below 200 °C. Several successive serpentinization events represented by different vein generations with distinct trace element contents can be recognized. Measured Rb/Cs ratios are fairly uniform ranging between 1 and 10, which is consistent with Cs mobilization from sediments at lower temperatures and lends further credence to the low-temperature conditions proposed in models of the

thermal structure in forearc settings. Late veins show lower fluid mobile element (FME) concentrations than early veins, suggesting a deacreasing influence of fluid discharge from sediments on the composition of the serpentinizing fluids. The continuous microfabric and mineral chemical evolution observed in the ultramafic clasts may have implications as to the origin and nature of the serpentinizing fluids. We hypothesize that opal and smectite dehydration produce quartz-saturated fluids with high FME contents and Rb/Cs between 1 and 4 that cause the early pervasive serpentinization. The partially serpentinized material may then be eroded from the basal plane of the suprasubduction mantle wedge. Serpentinization continued but the interacting fluids did not carry the slab-flux signature, either because FME were no longer released from the slab, or due to an en route loss of FMEs. Late chrysotile veins that document the increased access of fluids in a now fluid-dominated regime are characterized by reduced trace element contents with a slightly increased Rb/Cs ratio near 10. This lack of geochemical slab signatures consistently displayed in all late serpentinization stages may indicate that the slab-derived fluids have been completely reset (i.e. the FME excesses were removed) by continued water-rock reaction within the subduction channel. The final stage of diapiric rise of matrix and clasts in the conduits is characterized by brucite-dominated alteration of the clasts from the clast rim inward (independent of the intra-clast fabric relations), which corresponds to re-equilibration with alkaline, low-silica activity fluids in the rising mud.

Keywords: Serpentinization, polyphase alteration, mud volcano, fluid mobile elements recycling, hydrated mantle wedge, forearc peridotites, subduction zone.

1. Introduction

Subduction zones are sites of intense mass transfer between the subducting plate and the Earth's mantle. The incoming slab of oceanic lithosphere (sediments, as well as variably altered mafic and ultramafic rocks) releases a generally high but variable fluid flux (Bebout 2007). As a consequence of rheological contrasts between the juxtaposed rock-types, shearing and metasomatism evolve a complex mélange zone atop the slab (i.e., the subduction channel) where rocks and fluids are extensively modified (Cloos and Shreve 1988a, 1988b). The inventory of slab lithologies and the thermal structure determine where fluids leave the slab and where they enter the subduction channel (Schmidt and Poli, 1998; Reynard, 2013; Spandler and Pirard, 2013). In particular, the flux of fluids is affected by the local setting, e.g., the slab dipping angle and the presence, or absence, of an accretionary sedimentary wedge. During subduction, the downgoing slab progressively releases water (Hyndman and Peacock, 2006): at shallow depths by porosity compaction and dehydration reactions of sediments, at intermediate depths by dehydration of sediments and altered oceanic crust, and, at greater depths, by continued dehydration of oceanic crust and deserpentinization of the subducting lithospheric mantle (Schmidt and Poli, 1998; Rüpke et al., 2002, 2004). The geochemical signature of the fluids' source lithologies is recorded by fluids and rocks affected by subduction zone processes: fore arc springs, metasomatized melange material, serpentinized mantle peridotites, and arc volcanism inherit the distinctive trace element contents of the reacting fluids (Parkinson and Pearce, 1998; Fryer et al., 1999; Mottl et al., 2003, 2004; Savov et al., 2005a; Hulme et al., 2010).

Mud volcanoes are a characteristic feature of the forearc of the Mariana subduction zone system (Fryer et al., 1985; 1999; 2000). Located along the outer half of the

deeply fractured Mariana forearc, diapiric mud volcanism has formed large edifices from extrusion of blueschist and serpentine mud, up to 50 km in diameter and up to 2 km high (Fryer et al., 1990, 1999; Oakley et al., 2007). Systematic studies of pore waters and vent fluid compositions suggest that the fluids fueling the serpentine mud volcanoes are released from breakdown of hydrous phases in the subducting slab. Most noticeably, these fluids have lower chloride, Mg, Ca, Sr, Li, and Si concentrations, and higher pH, alkalinity, K, Na, Rb, Cs and Ba contents than seawater, indicating slab dehydration and water-rock interactions in the conduits feeding the mud volcanoes (Mottl, 1992; Benton et al., 2001; Mottl et al., 2003, 2004; Wheat et al., 2008; Hulme et al., 2010). The occurrence of blueschist fragments in the mud and rare metabasic clasts in the near-trench forearc region may indicate the involvement of upward migrating fluids and melange material in the subduction channel from deeper parts of the slab-mantle interface (e.g., Bebout, 2007). However, geobarometry on metabasite schists from South Chamorro Seamount (Fryer et al., 2006; 250-300 ℃ at a pressure of ~0 .4-0.50 GPa, ~12-15 km) and Conical Seamount (Maekawa et al., 1993; temperatures of ~175-250 ℃ and pressures of 0.5-0.65 GPa, ~15-19.5 km) indicate their origin in depths slightly above the base of the feeding conduits. Therefore, the erupted clast and mud materials record changes in the composition of the slab-sourced fluids, progressively released and accumulated in shallow and intermediate depths during subduction.

Trace element bulk rock compositions of serpentinized ultramafic clasts and serpentine mud have been used to gain deeper insights into the composition of the serpentinized forearc mantle (Savov et al., 2007; Deschamps et al., 2011), and to deduce potential parent rocks of the serpentinizing fluids (e.g., Hulme et al., 2010). At South Chamorro seamount, Ocean Drilling Program Leg 195 drilled Site 1200, where ultramafic clasts occur within the mud matrix (Straub and Layne, 2003; D'Antonio and Kristensen, 2004; Fryer and Salisbury 2006). These clasts record a

complex serpentinization history and provide an excellent window into the prevailing fluid-rock interactions at, and above, the interface between the mantle wedge and the subducting lithosphere. Moreover, the microfabrics of the highly serpentinized harzburgite and dunite clasts exhibit evidence for multiple fracturing events in the forearc mantle.

Here, we present a detailed investigation of trace element contents of the individual, successive serpentine generations and the primary mantle minerals. As many of these clasts have preserved domains representing early-stage serpentinization, we can reconstruct much of the history of fluid-rock reaction in the Mariana forearc and identify potential sources of the serpentinizing fluids.

2. Setting and samples

South Chamorro Seamount

Site 1200 is located on a knoll at the summit of south Chamorro Seamount in a water depth of 2930 m (Salisbury et al., 2002). Hole A was drilled with a rotary core barrel to a depth of 147.2 meters below seafloor (mbsf) and recovered mainly serpentinized ultramafic clasts and minor amounts of the mud matrix. South Chamorro Seamount (Fig. 1A) is one out of two dozen active mud volcanoes of the Mariana forearc, located 85 km west the trench where the Mesozoic Pacific Plate is being subducted west-northwestward beneath the West Philippine Plate (Fryer et al., 1990; Fig. 1B). The serpentine mud volcano was drilled in 2000 at Site 1200 of the Ocean Drilling Program (ODP) during Leg 195. Estimates of the slab depth beneath Site 1200 range between 26 km (Fryer, 1996; 1999) and 20 km (Oakley et al., 2005, 2007; Fryer and Salisbury 2006). The seamount is composed of unconsolidated flows of serpentine and blueschist mud with clasts of serpentinized mantle peridotite and

minor blueschist fragments (Fryer and Fryer, 1987; Fryer, 1996; Salisbury et al., 2002; Fryer et al., 2006). The mudflow matrix consists of c. 90 % serpentine, as clay- to silt-sized lizardite, chrysotile and minor antigorite. Accessory minerals of the mudflow matrix include brucite, talc, mixed-layer smectite/illite clays, chlorite, relict grains of primary silicates and Cr-spinel, amphibole and garnet. The sizes of clasts recovered from Site 1200 vary from a few mm to >1 m in diameter. The clasts represent lithologies from both the subducting plate and the suprasubduction-zone mantle. In Hole 1200A, the peridotite clasts are predominantly harzburgites and minor dunites. Serpentinization is extensive and ranges between ~40 % and 100 % with an average alteration of 95 % for harzburgites and 75 % for dunites (D'Antonio and Kristensen, 2004).

In this study, nine samples from the marginal parts of highly serpentinized clasts of harzburgite and dunite were selected for detailed petrographic and microanalytical geochemical investigations (Table 1). A second set of adjacent samples from the clasts' centers was chosen for thin section microscopy to identify the mineralogical and textural differences between clasts' rims and cores (Table 1).

3. Analytical methods

Petrography

Mineral phases were identified by polarized light microscopy. In addition, a *Panalytical X'Pert PRO* X-ray diffractometer (XRD) at the University of Bremen (Cu Kα radiation, 45 kV, 40 mA) was used to identify serpentine modifications in the samples selected for oxygen isotope analysis (see below). Data were collected in the continuous mode, between 3 to 85 °2θ, in steps of 0.017 °2θ. Spectra were processed with *High-Score Plus* software.

Electron microprobe

Major element analyses of mineral compositions were performed with a *JEOL JXA-8900* electron microprobe at the University of Kiel (Germany). For most silicate minerals an accelerating voltage of 15 kV was used, with exception of garnet, spinel and iron oxides (20 kV). Measurement spot sizes were typically 1-5 µm in diameter. Standards were either natural minerals or synthetic materials. The CITZAF method of Armstrong (1995) was used for correction of the raw counts. Micro-scale element mappings and backscattered electron (BSE) images of rock microfabrics were used to complement microscopic observations.

Laser ablation ICP-MS

Analyses of major and trace element concentrations were carried out on thin sections by laser ablation inductively coupled plasma mass spectrometry (LA-ICP-MS) using a Thermo Element2 coupled to a NewWave UP193ss (wavelength 193 nm) at the Department of Geosciences of Bremen University. Helium (0.8 l/min) was used as carrier gas and argon (0.8-0.9 l/min) was added as make-up gas; plasma power was 1200 W. Samples and standards were ablated with an irradiance of ~1 GW/cm^2, and a pulse rate of 5 Hz. The laserbeam diameter was typically between 25 and 100 µm. Prior to ablation the blank intensities were acquired during 25 s. All isotopes were analyzed at low resolution with five samples in a 20% mass window and a total dwell time of 25 ms per isotope. Depending on the mineral composition, either silicon or magnesium was used as an internal standard element, which had previously been determined by electron microprobe analysis. Calibration was done using glass standards NIST610 and NIST612, with preferred averages from Jochum et al. (2011). Analytical quality was controlled by repeated analyses of the international glass standard BCR2-G (Jochum et al., 2006).

Micro-Raman invstigations

Serpentine phases were identified using a Horiba LabRAM HR confocal Raman spectrometer equipped with a 532 nm laser, an astigmatic flat field spectrograph with a focal length of 800 mm, and a multichannel air-cooled (-70 ℃) CCD detector. Spectra were collected using a 100x objective with a numerical aperture of 0.9. Two diffraction gratings with 600 and 1800 grooves / mm were used. A confocal hole diameter of 100 μm was chosen for most analyses. Spectra were collected for 5 seconds with 3-5 accumulations between 100 cm^{-1} and 1280 cm^{-1}.

Oxygen isotope analysis

For oxygen isotope analysis, serpentine minerals of the different generations were separated by crushing and hand picking, and purity and mineralogy were checked by X-ray diffraction (see above) and visual inspection. The oxygen isotope analyses were carried out at the University of Michigan following the procedure of Alt et al. (2010). Samples were reacted with BrF_5 in externally heated nickel reaction vessels (Clayton and Mayeda, 1963), and O_2 was converted to CO_2 gas by reaction with heated carbon rods. Oxygen isotope ratios were measured using a Finnigan Delta-S mass spectrometer. These data were normalized to a value of 9.6‰ for NBS 28 quartz standard (± 0.2‰, 1σ), compared to the accepted value of 9.58 ‰.

4. Results

The observations presented here are based on nine extensively serpentinized harzburgite and dunite clasts sampled from different depth intervals of Hole 1200A (see Table 1). In particular, the clast material selected for thin section preparation and analytical investigation was collected from near-rim regions that show considerable influence of late-stage alteration events.

4.1 Petrography

The serpentinized ultramafic clasts exhibit a variety of microfabrics that range from virtually undeformed to strongly deformed (see Figs. 2 and 3). The degree of serpentinization we observed in thin section varies between 75 % and almost 100 %, but can be highly variable on the scale of centimeters. Even within the same thin section, weakly serpentinized regions can be observed adjacent to regions with abundant veins of different generations.

Relicts of primary olivine with average grain diameters of around 50 μm (some grains are up to 250 μm in diameter) show microgranulation and kink-banding in some areas. The size of the original olivine grains in the precursor rock was up to 3 mm. Relicts of orthopyroxene show signs of crystal deformation (undulary extinction and cleavage planes); former grains were up to 4 mm in size. Clinopyroxene is preserved as solitary crystals (diameter up to 100 μm) either in proximity to orthopyroxene, or intimately intergrown with chromian spinel. In addition, clinopyroxene is present as exsolution lamellae in orthopyroxene. In a dunite sample, spinel exhibits rhomb-shaped euhedral faces, whereas in the harzburgites studied it commonly shows embayments indicative of resorption.

Fabric relations

Serpentinization of the primary minerals led to pseudomorphic mesh and hourglass textures after olivine and bastite after orthopyroxene (and locally of clinopyroxene). Serpentine is present in veins of several generations. Besides serpentine group minerals, brucite is a common secondary phase. It is observed in intimate

intergrowth with serpentine in veins, and as single crystals in the centers of recrystallized mesh textures.

Heazlewoodite and awaruite (Ni_3Fe) are present in trace amounts. The atomic metal/sulfur ratio of heazlewoodite is near stoichiometric and varies between 1.59 and 1.68. Small amounts of Fe account for a representative composition of $(Ni_{2.97}Fe_{0.03})S_2$. Heazlewoodite can be present in the centers of hour glass structures, or as rare occurrence in veins, rimmed by awaruite. Moreover, awaruite is observed on trails in the center of serpentine veins in mesh-textured olivine (Figs. 3A and B). Awaruite and in a few instances wairauite (CoFe) are present in halos around type (i) veins and in type (ii) veins (vein types as detailed below). Magnetite is developed in early veins, which predate pervasive serpentinization as characteristic (double) central vein filling (D'Antonio and Kristensen, 2004; Klein et al., 2009). Furthermore, magnetite was found in late, extension-related veins as syntactically grown crystals. Garnet of andraditic composition (with neglectable Al and Mg contents, and with a hydroandradite (hydrogarnet) component, calculated from Si deficiency) is present in two samples. It is either homogeneously distributed as small euhedral crystals (up to 50 μm in diameter) or clustered in anhedral crystals (individual crystals up to c. 70 μm, clusters up to 300 μm). In either case, garnet growth was located in mesh-textured domains, commonly at the boundary between mesh core and rim. Apparently, those parts of the grains growing into the mesh core developed anhedral morphology, contrasting with the euhedral habit of the faces that grew towards the mesh rim. A representative garnet composition is $(Ca_{2.98}Mg_{0.04})(Fe_{1.98}Al_{0.01}Cr_{0.00})(Si_{2.81}H4_{0.19})O_{12}$, the hydroandradite component shows values between 0.14 and 0.27.

Pervasive serpentinization

Pervasive serpentinization of olivine resulted in the formation of mesh (with fresh olivine in the cores) or hourglass textures (see Figs 2, and 3A and B). Former olivine grain boundaries in mesh textures are outlined by awaruite; in most samples the mesh texture is free of magnetite. Pseudomorphic serpentinization of orthopyroxene (and locally of clinopyroxene) led to the formation of bastites. Former interstitial spinel is apparently unaffected by alteration and is (in places) surrounded by serpentine coronae formed from breakdown of orthopyroxene and olivine (as described by Seyler et al., 2001). Brucite was not observed in pervasive mesh textures. However, it is present in interstices between clinopyroxene (sub)grains, in regions of mesh textures that were affected by vein serpentinization, or recrystallized hourglass textures (see Figs. 2A, 2G). Serpentine in mesh textures and bastites has been identified as lizardite by Raman spectroscopy (for serpentine polymorphs identified in the polyphase serpentinization fabrics, see Table 4), which is consistent with investigations of similar textures in other serpentinites (e.g., Dilek et al., 1997; Andreani et al., 2007; Boudier et al., 2010; Pabst et al., 2011; Schwartz et al., 2012).

Veins

The most striking fabric element present in the clasts is the abundant veining, which comprises different vein generations.

In harzburgites, several stages of veining and associated serpentinization can be distinguished:

Early magnetite-bearing veins (predating pervasive serpentinization)

Serpentine veins containing magnetite were found in one of the thin sections studied (see Fig. 2A). In these transgranular veins magnetite occurs as central vein fillings or as double trails along the vein rim. This fabric type has been reported in other

ultramafic clasts recovered from Site 1200 (e.g., D'Antonio and Kristensen, 2004), as well as in serpentinized abyssal peridotites from the Mid-Atlantic Ridge (recovered from Leg 209, Hole 1274A, see Klein et al., 2009). These veins are likely an early feature, preceeding and maybe initiating the pervasive serpentinization of pristine ultramafic rock (Salisbury et al., 2002).

Type (i) veins

This vein type postdates pervasive serpentinization and features lizardite with brucite and awaruite; veins are straight without marked conformance with the rock fabric (see Fig. 2D1, and 2E). The walls of type (i) veins may show finger-like serpentinization fronts. These "fingers" seem to emanate into interstices of mesh textured domains formed during a preceeding pervasive serpentinization event. In places, these veins developed mm- to cm-wide halos. In places, veins of type (i) have been reactivated by later fluid fluxing events of type (iv) veins.

Type (ii) veins

These chrysotile-brucite veins (Table 4) encompass regions of weakly serpentinized, microgranular olivine and large orthopyroxene crystals (Fig. 2B-E). They are brownish in color and up to 2 mm wide. Type (ii) veins do not show a preferred orientation and appear to have formed to accomodate expansion which is not related to expansion during pervasive serpentinization. However, the orientation of the fibers with respect to the vein walls documents an anisotropic stress field. It is unclear, whether this feature represents growth or recrystallization of the vein serpentine.

Type (iii) veins

Extensional chrysotile veins (known as "Frankenstein" type, see e.g., Salisbury et al., 2002) have developed in halos along type (i) veins (where they may intersect type (ii) veins; Fig. 2D, 2E, and Table 4). They are related to the accomodation of local

stresses during the overall isotropic expansion of the surrounding rock. A similar vein geometry has been described in detail from serpentinized orthopyroxenite dykes in a dunite matrix from the Leka Ophiolite Complex, Norway (Iyer et al., 2008a, 2008b).

Type (iv) veins

Late-stage extensional chrysotile veins document multiple crack-seal events (as described by Bons et al., 2012) either in undeformed regions with preserved granular fabric, or in serpentinites hosting type (i) and (ii) veins where they crosscut and offset the earlier vein generations (see Fig. 2F).

Extensional magnetite-bearing veins

One thin section contains magnetite, present in deformation-related extensional veins, which developed as syntaxial veins from a single crack-seal event. Large crystals extend from one wall to the other (as confirmed with high-resolution X-ray microtomography).

Some dunites host syntaxial serpentine veins (ribbons). The ribbons separate regions, in which recrystallization of serpentine and brucite can be observed (see Fig. 2G). The extension accommodated by the ribbons is clearly anisotropic.

Late Browning

A "browning" of the clasts' margins is developed in few samples (e.g., 3R-1, 7R-2, 13R-2, 16R-1), which is related to an inward-migrating alteration front (Fig. 2H). This browning is independent of the intra-clast fabric relations comprised by the different vein generations. Browning led to high proportions of brucite in the rock that proceeded either localized along former grain or sub-grain boundaries or in a

pervasive manner. The latter may develop by coalescence of grain boundary scale replacement.

4.2 Mineral chemistry

Primary minerals

Olivine in both harzburgite and dunite is Mg-rich (X_{Mg} = [Mg/(Mg+Fe)] of 0.92) (Figs. 4A-D, Table 2), which is typical for mantle wedge peridotite (Bonatti and Michael, 1989; Ishii et al., 1992). Orthopyroxene has X_{Mg} values between 0.91 and 0.92, Al_2O_3 contents from 1.3 to 2.5 wt.%, and contains 0.6 to 1.2 wt.% Cr_2O_3 (see Figs. 4A-D, and 5A-C). X_{Mg} ratios of clinopyroxene range between 0.94 and 0.95, with 0.96 - 2.02 wt.% Al_2O_3, and 0.24 - 1.09 wt.% Cr_2O_3. Chromian spinel is variable in composition with X_{Cr} [Cr/(Cr+Al)] values between 0.48 and 0.63, and X_{Mg} ranging from 0.51 to 0.59 in the pervasively serpentinized regions in harzburgites.

In the two most strongly serpentinized harzburgites and dunites (9R-1 and 11R-1), spinel approaches ferritchromite composition (X_{Cr} = 0.69 - 0.93 and X_{Mg} = 0.22 - 0.43). Ferritchromite is commonly regarded as an indicator of Cr-spinel alteration (e.g., Mellini et al., 2005; Merlini et al., 2009; Saumur and Hattori, 2013).

Serpentine minerals

The polyphase serpentinization history of the ultramafic clasts is apparent in distinct mineral compositions of the successive serpentine generations (Figs. 4A-D and 5A-C). Pure chrysotile/lizardite has a molar ($Mg+Fe^{2+}$)/Si ratio of 1.5. However, since the majority of serpentine mineral EMPA analyses of the early vein generations of type (i) and (ii) exhibits significantly lower SiO_2 and higher MgO contents, it appears that minor brucite is intergrown with serpentine on a submicroscopic scale (Table 3).

Compositions of pseudomorphic serpentine minerals formed during the pervasive serpentinization phase were found to be indicative of their precursor mineral in terms of Al_2O_3 and CaO contents of the serpentine phase (Fig. 5A-C). Serpentine in mesh and hourglass textures has X_{Mg} values of 0.90 - 0.94. Serpentine in mesh and hourglass textures does contain as little Cr_2O_3 as the olivine precursor, but exhibits higher Al_2O_3 and CaO as olivine. These serpentines in harzburgites (Al_2O_3 > 0.1 to < 1.0 wt.%, CaO: 0.1 - 0.6 wt.%) tend to be richer in both components than dunites (Al_2O_3 < 0.1 wt.%, CaO: 0.08 - 0.2 wt.%). In recrystallized hourglass textures in dunite, the X_{Mg} of serpentine coexisting with brucite is slightly higher (0.94-0.96) than X_{Mg} of serpentine in unrecrystallized regions. No differences between mesh rim and core compositions have been observed. Bastite textures consist of serpentine, with X_{Mg} values between 0.89 - 0.94. Most bastites retain the high Al_2O_3 contents (> 1.0 wt.%), as well as the CaO (0.1 - >1.0 wt.%) and Cr_2O_3 (0.1 - 1.0 wt.%) values of the pyroxene precursor (see Fig. 5A-C). Analyses of serpentine in halo regions of type (i) veins and in type (ii) veins show marked SiO_2 deficits (Fig. 4B-C), indicating intergrowth with submicroscopic brucite, and low X_{Mg} values (an average X_{Mg} of 0.80 in Brc-Srp intergrowth, and down to X_{Mg} of 0.40 in coexistence with Cpx). Serpentinites in the halos of type (i) veins show identical contents of Al_2O_3 and CaO as the pseudomorphs outside the halos. Serpentine in type (iii) and type (iv) veins shows SiO_2 contents expected for pure serpentine and X_{Mg} values of 0.89 - 0.96 (see Fig. 4D). Later veins of type (ii)-(iv) also exhibit the characteristic Al_2O_3 and CaO contents of the pseudomorphs present in their host rocks (see Fig. 5A-C).

Using Micro-Raman investigations of the polyphase serpentinization fabrics, we have identified two serpentine polymorphs: Lizardite and chrysotile (see section 4.1 and Table 4). Lizardite has been found in the rims of mesh textures, surrounding olivine cores, and in bastites. Moreover, it is present in mesh/hourglass and bastite pseudomorphs in regions that were affected during the halo formation around type (i)

veins. Later vein generations (type ii-iv) are comprised of chrysotile. In the clasts investigated by micro-Raman, no antigorite was identified.

Brucite

Brucite is present either as readily identifiable crystals (up to 100 μm diameter) in interstices or recrystallized areas, or fine-grained as vein fill. The occurrence of brucite submicroscopically intergrown with serpentine minerals has been recognized from microprobe analyses based on SiO_2 deficits, MgO excesses, and low totals (see above, and Table. 3). Brucite-serpentine intergrowths in harzburgites were also observed in type (i) and type (ii) veins and point to brucite compositions of $X_{Mg,Brc}$ 0.79 - 0.85. Brucite is apparently lacking in the pervasive serpentinization stage as well as in type (iii) and in type (iv) veins.

In harzburgites, interstitial brucite is present in type (i) veins or halos, typically with MnO contents from 0.19 to 0.53 wt.%, and X_{Mg} values between 0.79 and 0.90. In places, type (i) veins contain brucite with slightly elevated MnO contents between 0.94 and 2.20 wt.% and low X_{Mg} values of 0.59 - 0.63 (these MnO values correspond with brucite analyses given in D'Antonio and Kristensen, 2004). A single occurrence of brucite in contact with clinopyroxene features 1.65 to 2.19 wt.% MnO and X_{Mg} values between 0.36 and 0.47. In dunites, single crystals of brucite can be observed where cores of hourglass textures have recrystallized (Fig. 2G). The X_{Mg} values of the recrystallized brucite range between 0.83 to 0.85.

4.3 Trace element mineral chemistry

Trace element concentrations of serpentine provide insights into potential precursor phases and compositions of serpentinization fluids.

Ni and V contents of serpentine are different for olivine and pyroxene precursors. Figure 6A shows that serpentine (or regions of serpentine-brucite intergrowth) formed at the expense of olivine can contain up to 0.5 wt.% Ni (with an average around 0.3 wt.%), corresponding to the Ni content of the primary olivine. Or rather, Ni is most likely measured as fine-grained awaruite, present in the laser-ablation spots). In contrast, bastite-serpentine (i.e. orthopyroxene precursor) has < 0.1 wt.% Ni, corresponding to the average Ni concentration of ortho- and clinopyroxene (c. 700 ppm). Likewise, V concentrations of serpentine (Fig. 6B) replacing olivine are mostly below 1 ppm, which reflects the V concentration of its precursor. In bastite textures, V contents are up to 80 ppm, corresponding to 60-80 ppm V in orthopyroxene. On rare occasions, bastitization of clinopyroxene has been observed in completely serpentinized clast rims (identified by the shape of the former grain). Here, vanadium contents are slightly higher as in orthopyroxene bastites (60-120 ppm). The Ni-V variation diagram (Fig. 6C) shows the discriminatory significance of these trace elements in identification of the serpentine parent mineral. The variation in the Cr-Ni diagram (not shown) is identlical apart from the higher absolute concentrations of chromium (section 4.2), corresponding with data from Kodolanyi et al. (2012).

B, Ba, Sr, Rb and Cs data of regions with submicroscopic intergrowth of serpentine and brucite show increasing trace element concentrations with increasing Si/(Mg+Fe)-ratio, which indicates that these elements are incorporated in the serpentine structure and are not present in brucite (Figs. 7A-E). Therefore, the element concentrations of the mixed analyses of serpentine-brucite regions have been recalculated to pure serpentine (indicated by the curved lines in Figs. 7A-E).

Regardless of the nature of the precursor phase and presumed formation stage, all serpentinization products are enriched in B (Figs. 7A and 7F), and calculated

serpentine endmember compositions have up to 200 ppm boron (mostly between 80-100 ppm). Ba, Sr, Rb, and Cs are also commonly enriched in the serpentinization products and veins relative to the precursor phases (Fig. 7B-E). In contrast to B, however, these elements show distinct differences in concentration between serpentine formed during different stages of veining and fluid-rock interaction. Most notably, early vein generations show high trace element concentrations compared with later veins (Table 4).

On average, serpentine of the early serpentinization stages (i.e., in mesh rims of pervasive stage, in type (i) veins, or in the halo around type (i) veins) exhibit a strong enrichment in Rb (0.8 ppm), Cs (0.4 ppm), Ba (> 10 ppm), and Sr (> 50 ppm). For Ba and Sr the enrichment is unrelated to the nature of the precursor mineral, while bastites, and interstitial serpentine of regions with only weakly serpentinized orthopyroxene and microgranular olivine crystals, have even higher concentrations of Rb (up to 2.6 ppm) and Cs (up to 1.2 ppm; Figs. 7D and E). In the later vein generations, remarkable differences in the enrichment of either (Rb and Cs) or (Ba and Sr) occur. In type (ii) veins, average Ba (3.7 ppm, up to 11.3 ppm) and Sr (13.6 ppm, up to 27.7 ppm) concentrations are also high. In type (iii) and (iv) veins, serpentines show average concentrations of Ba (0.4 ppm) and Sr (3 ppm), which markedly lower than in the earlier vein generations (types i and ii), but still significantly higher than those of the primary minerals (Figs. 7B and C). In contrast, the average concentrations of Rb and Cs in serpentines of type (ii)-(iv) veins are low (<0.1-0.3 ppm) and similar to those of the primary phases Figs. 7D and E).

4.4 Oxygen isotope compositions of serpentine minerals

The measured oxygen isotope compositions of serpentine minerals range between 6.1 and 10.5 $\delta^{18}O$, consistent with serpentinite clasts from Conical, Torishima, and Ogasawara Seamounts (Alt and Shanks, 2006; Sakai et al., 1990). Table 5 provides an overview of the oxygen isotope data for the mineral separates along with details about mineralogical composition of the different samples (as determined by XRD analyses). The oxygen isotope data do not show significant differences between different vein generations or serpentine polymorphs. Note that two mineral separates contained a noticeable fraction of brucite (16R-2).

5. Discussion

5. 1 Low-temperature serpentinization conditions in the Mariana mantle wedge

The serpentinized ultramafic clasts exhibit a variety of microfabrics that indicate a polyphase serpentinization history. A common feature during all stages of serpentinzation is that little magnetite was formed (if at all). In contrast to samples from mid-ocean ridge settings, mesh textures lack magnetite tracing former olivine (sub-)grain boundaries. Instead, the serpentinized ultramafic clasts are composed of serpentine ± brucite ± iron alloys (mostly awaruite). This magnetite-free assemblage has been found as late-stage formation in rocks from magma-poor rifted continental margins (Beard et al., 2009), in the forearc of subduction zones (Lafay et al., 2012), and in low-temperature serpentinization experiments (batch reactor: Seyfried et al., 2007; flow-through experiment: Godard et al., 2013). In a recent study, Klein et al. (2014) propose that decreasing abundance of magnetite is indicative of decreasing alteration temperatures. Instead of magnetite, Fe-rich brucite forms at temperatures below ca. 200℃ (cf. Klein et al., 2009). These low formation temperatures would be consistent with temperatures predicted for a depth of 25 km by models of the thermal

structure of a cold oceanic subduction zone (Izu-Bonin, see Hyndman and Peacock, 2003).

Metabasite clasts may serve as an additional constraint on p,T-conditions that prevail at the slab-mantle interface recorded at variable depth levels reaching from intermediate to near the base of the conduit of the mud diapir. In the case of South Chamorro Seamount and Conical Seamount, metabasite schists indicate low temperatures of 250-300 ℃ (at a pressure of •0.4-0.50 GPa; Fryer et al., 2006) and ~175-250 ℃ (at a pressure of 0.5-0.65 GPa; Maekawa et al., 1993), in depths slightly above the base of the feeding conduits.

The δ18O values for serpentine in this study (6.1 to 10.8 ‰) are similar to those from Conical seamount and to those dredged from Torishima and Ogasawars Seamounts (Sakai et al., 1990; Alt and Shanks, 2006). Using oxygen isotope fractionation between serpentine and magnetite, Alt and Shanks (2006) calculated higher temperatures of 300-375 ˚C for serpentinite clasts from Conical Seamount. The dominance of antigorite in some of the Conical Seamount samples suggests that higher estimated temperatures may be real, as antigorite is stable at higher temperatures (above 300 ˚C, Schwartz et al., 2012), but these temperature estimates were based on mineral separates from bulk rocks (Alt and Shanks, 2006), which integrate multiple stages of serpentinization and magnetite formation, leading to larger uncertainties. In the rocks studied in this work, no pairs of coexisting serpentine and magnetite were at hand for temperature estimation. Since the presence of magnetite is restricted to scarce occurrence in vein types not related to the main serpentinization phases (see above), it is not very likely, that a magnetite separated from bulk rock powders would be coeval with chrysotile separated from late veins. Rather, fluid-rock ratios, the fluids as such, and maybe also the temperatures prevalent at early mesh formation (yielding magnetite, given

appropriate conditions) would differ from late-stage conditions governing the formation of late-stage, extensional chrysotile veins. However, by constraining some boundary conditions for the fluid-rock interaction we can estimate serpentinization temperatures of the 1200A clasts.

Using the serpentine-water oxygen isotope fractionation from Saccocia et al. (2009), temperatures of 175-240 ˚C are calculated assuming equilibrium between serpentine in Table 5 and fluids sampled from South Chamorro seamount ($\delta^{18}O$ = +2.5‰; Fryer et al., 2006). Lower temperatures of 145-200 ˚C are calculated assuming equilibrium with seawater (0‰). Stable isotope compositions of serpentinites from Conical seamount indicate derivation of serpentinizing fluids from the subducting slab (Alt and Shanks, 2006). If serpentinizing fluids contained a component of sediment pore waters, which have negative $\delta^{18}O$ values (Lawrence and Drever, 1981), then equilibrium temperatures for serpentine are even lower (125-170 ˚C for -2‰ fluid; Saccocia et al., 2009). These temperature estimates are consistent with low temperatures inferred from mineralogy of Chamorro samples and with thermal models for cold subduction (Klein et al., 2009; Hyndman and Peacock, 2003).

The above estimates suggest relatively low temperatures (below 250 ℃) for the serpentinite samples from South Chamorro seamount (Site 1200, distance from trench: 85 km), which seemingly is in contrast to the higher serpentinization temperatures of 300 - 375 ℃ estimated for samples from Conical seamount (Site 780, distance from trench: 90 km; distance from Site 1200: almost 1000 km) by Alt and Shanks (2006). While the high-temperature polymorph antigorite is the dominant serpentine phase in several samples from Conical seamount, it is scarce in South Chamorro and other Mariana forearc seamounts (see section 5.2). On the contrary, the absolute concentrations of Cs, Rb, Ba, and Sr observed in serpentine in this

study indicate that the serpentinizing fluids of the South Chamorro samples derive from sediment dehydration at temperatures of ~ 150 ℃ (section 5.3), similar to the estimations by Alt and Shanks (2006) for Conical. We consider this an expression of both a differing subduction zone geometry and the variation in the thermal structure of the slab and wegde: the mud volcanoes can sample the entire thickness of the wedge, and can include samples from any time within the 40 million year history of the subduction zone. So they could include early higher-temperature serpentinites, which could be one explanation for high-temperature samples at Conical seamount. Certainly in a "mature" subduction zone, without mantle counterflow in the wedge, the low temperatures as shown by the Chamorro samples are expected. Moreover, the source region of the ultramafic material mobilized as clasts and erupted in mud flows does not necessarily lie within the wedge. Besides serpentinization of conduit wall rock, also material from the basal plane of the suprasubduction mantle wedge, partly serpentinized and eroded in shallower parts of the decollement, may rise through the conduit system and be erupted within the mudflows (section 5.4).

5.2 Textures and serpentine polymorphs

Different low-temperature serpentine polymorphs are common in serpentinized abyssal peridotites. In the present work, micro-Raman investigations demonstrate the occurrence of two serpentine polymorphs in distinct textural context. Lizardite is present in the rims of mesh textures, surrounding olivine cores, in bastites, and in early type (i) veins. Later vein generations are comprised of chrysotile. Antigorite, which is commonly seen as indicative for higher-temperature serpentinization, could not be identified. In previous studies of ultramafic clasts from ODP Leg 195, Site 1200 (D'Antonio and Kristensen, 2004; Pabst et al., 2011), lizardite and chrysotile, but not antigorite, were identified. At Conical Seamount, Ishii et al. (1992), and

Saboda et al. (1992) observed antigorite in thin sections of serpentinized dunite (Hole 780C) and harzburgite clasts (Hole 779A). Alt and Shanks (2006) observed antigorite in serpentinized harzburgites and dunites from Site 779 and 780, being the dominant serpentine phase in several samples. In contrast, antigorite was putatively identified by Fryer and Mottl (1996) in muds at Holes 778A and 779 A (in 3 out of 16 samples) but appears absent in Site 780 muds. As stated in Savov et al., (2005a), scarcity or absence of antigorite in the Mariana forearc serpentinites (apart from Conical Seamount) are noted by many authors (e.g., Saboda et al., 1992; Zack et al., 2004; Murata et al., 2009; Pabst et al., 2011), while chrysotile and lizardite are common.

In numerous studies of oceanic serpentinites, the growth of distinct serpentine polymorphs under different reaction conditions (e.g., varying water rock ratios, tectonic regimes etc.) was noted. For instance, lizardite in rims around olivine mesh centers, and in bastites, has been reported from the mid-ocean ridge Site 920, e.g., by Dilek et al., (1997, by XRD), Andreani et al., (2007, by TEM; 2013, by Raman), from Sites 1272 and 1274 by Kodolanyi et al., (2012, by Raman), and from ophiolites, e.g., by Boudier et al., (2010, TEM), Hirauchi et al., (2010, Raman), and Schwartz et al., (2012, Raman). The clasts from Mariana forearc mantle may exhibit a great diversity with respect to (i) the differing degree of serpentinization, (ii) the differences in the source regions within the mantle wedge, and (iii) the relative timing of serpentinization stages in the individual clasts. Pabst (2009) found either lizardite or chrysotile both in mesh rims and mesh centers, and also the occurrence of polygonal serpentine is reported. Pabst (2009) found bastites composed of lizardite, in other samples of polygonal serpentine. Kodolanyi et al. (2012) reported the occurrence of lizardite in mesh rims and bastites, and of chrysotile in mesh centers and bastites. In the present study, lizardite has been found in early serpentinization textures, and chrysotile in intermediate and late vein generations.

In most of the aforementioned studies, chrysotile has been found in extensional veins, crosscutting pervasive serpentinization and in earlier vein generations. Furthermore, Andreani et al., (2007, 2013), mention the involvement of polygonal serpentine in the vein mineralization. In general, the preferential occurrence of chrysotile in expansional regimes with higher water-rock ratios has also been noted for the ultramafic clasts from the Mariana forearc mud volcanoes (e.g., D'Antonio and Kristensen, 2004; Pabst et al., 2011; and described in more detailed by Pabst, 2009).

In the present study, the pseudomorphic serpentinization textures suggest that early pervasive serpentinization took place under static conditions (e.g., Wicks and Whittaker, 1977; O'Hanley 1996), yielding isotropic expansion. In the course of the successional veining events, the expansional regime gradually became more anisotropic. The formation of type (i) veins points to clearly anisotropic stress, however related to merely minor expansion. Type (ii) veins do not show a preferred orientation and appear to have accomodated considerable overall isotropic expansion. The extensional chrysotile veins of the "Frankenstein" type (iii) veins accomodate local stresses in the halos along type (i) veins, associated with the overall isotropic expansion of the surrounding rock. Late-stage extensional type (iv) chrysotile veins formed in a clearly anisotropic stress regime and led to anisotropic expansion, documented as multiple crack-seal events (as described by Bons et al., 2012).

5.3 In-situ mineral analyses reveal distinct FME patterns for successive serpentinization events and potential fluid source rocks

Since the proportions of the different serpentine generations in the bulk sample and the fraction of brucite in Srp-Brc intergrowth regions are highly variable, it is difficult to unravel the formation history of the clasts using trace element contents of bulk rocks. For instance, Savov et al., (2007) observed no correlation between the degree of serpentinization (expressed as LOI wt.%) and the abundance of FME and Th. The detailed mineral analyses of serpentine, in contrast, facilitate the recognition of different trace element contents in distinct veins and microfabrics, which can be linked to distinct episodes in the polyphase serpentinization history of mantle material.

The observed trace element contents in the clasts from South Chamorro Seamount decrease with progressive serpentinization. These elements are incorporated in the serpentine structure and are not present in brucite (Figs. 7A-E; section 4.3). While later serpentinization stages recorded in the clasts - and the trace element concentration measured in serpentine of the mud matrix - are characterized by decreased FME concentrations, both bastites and interstitial serpentine in microgranular olivine regions formed during preceding serpentinization events share higher FME contents.

In order to explain the observed variation of serpentine trace element concentrations, selected mineral analyses are compared with literature data on related bulk rock and fluid compositions (Fig. 8). Concentrations of Cs and Rb (Fig. 8A) from the late serpentine type (iii) and type (iv) are similar to the Cs/Rb values reported by Savov et al. (2007, and 2005) for the mud matrix. In contrast, products of all earlier veining and serpentinization events yield higher Cs and Rb values, which are similar to the variation of bulk compositions reported by Savov and coworkers for the serpentinized clasts. The same systematic difference can be seen in the concentrations of Sr and Ba (Fig. 8B). Trace element contents of sediments (from Plank and Langmuir, 1998)

and variously altered oceanic crust (AOC; Kelley et al., 2006) as potential source rocks of the serpentinizing fluids are also plotted in Fig. 8, together with analyses of "fresh peridotite" from Meffré et al., (2012).

Rb, Cs, Sr, and Ba concentrations in sediments are higher than in both mud matrix and serpentine veins in the clasts. Altered oceanic crust (AOC) may have higher Sr and Ba contents than either mud matrix or clast serpentine, and may show similar Cs contents as the mud matrix and serpentine in clasts, depending on the alteration stage. However, AOC contains slightly less Cs than the early clast serpentine generations. In contrast, Rb concentrations of strongly altered oceanic crust may be higher than those of mud and late clast serpentine, and even higher than those of early clast serpentine generations. Thus, both sediments and altered ocean crust could serve as source for higher Sr and Ba values in the serpentinizing fluid, but only sediments and very highly altered oceanic crust can be considered to discharge high Cs,Rb fluids. The main sources of fluid to be released in a low-T environment such as the forearc region of a cold subduction zone are thought to be related to sediment compaction and from sediment dehydration reactions involving opal (at 30 - 80 ℃) and smectite (120 - 150 ℃; see Hyndman and Peacock , 2003; Fryer and Salisbury, 2006), with little or no participation of AOC as fluid source.

The mobilization of volatiles (B and NH_4) and incompatible elements (As, Be, Cs, Li, Pb, Rb) in hydrothermal fluids at relatively low temperatures (~ 300 ℃) was demonstrated by You et al. (1996) in laboratory hydrothermal autoclave experiments with sediments of the decollement zone at Site 808 in Nankai Trough, Japan. The absolute concentrations of Cs, Rb, Ba, and Sr observed in serpentine in this study, indicate that fluids derived from sediment dehydration may account for high trace element contents in serpentine formed during the pervasive stage and the early vein generations. Regardless of the absolute Cs and Rb contents of lizardite and

chrysotile, the observed Rb/Cs ratios are fairly uniform within the different serpentine generations and average between 1 and 10 (average Rb/Cs ratios in early serpentines (mesh, bastites, vein types I and II) are between 2-4, associated with high absolute elemental concentrations; late serpentine exhibits averaged Rb/Cs ratios of 7 (type III) and 8 (type IV), associated with low absolute elemental concentrations; Fig. 8A). It is possible that subducted sediments containing a high fraction of pelagic clays release fluids high in Rb and Cs, and account for the high trace element contents of serpentine formed in the pervasive stage and the early vein generations. The uniformly low Rb/Cs ratios ≦10 observed in the serpentine minerals from Site 1200A are consistent with a sedimentary origin of the serpentinizing fluids, which were released at low to moderate temperatures (50 - 300 ℃), indicating a higher mobility of Cs relative to Rb.

The systematic variation of trace element contents of pore fluid compositions of several seamounts with distance from the Mariana trench, revealed in geochemical studies (Fryer et al., 1999; Mottl et al., 2003, 2004; Hulme et al., 2010), support the hypothesis of sediments as a main source of slab fluids in the forearc region. Figures 8A and 8B shows the trace element contents of the pore fluids from South Chamorro and other Mariana forearc seamounts as summarized in Mottl et al. (2004). Water compositions from the following seamounts, in the order of increasing distance from the trench, are also plotted: Bottom seawater (distance: 0 km), Pacman Baseball Mitt (52 km), Blue Moon (55 km), Pacman summit (64 km), Big Blue (70 km), S. Chamorro S351 spring (85 km), Seamount Site 1200 (85 km), and Conical Site 780 (90 km). The observed concentrations are consistent with increased mobilization of trace elements from sediments with increasing temperature and depth of slab, as predicted for cold subduction zones (Hyndman and Peacock, 2003; Plank and Langmuir, 1998; Fryer, 2012, and references therein). The accuracy of these

predictions is also supported by the similarity of the fluids in terms of Rb and Cs (Fig. 8A) observed in the experimental charges of You et al. (1996). The Ba concentration might be influenced by complex interactions with sulphate (Fig. 8B). Admittedly, although the fluids discharged in experimental runs document the mobilization of trace elements from solids into the fluid phase, the fractionation of trace elements into the secondary minerals during serpentinization is unknown. However, as indicated by the similarity in trace element contents of late-stage vein and mud serpentine, the fluids constituting the mud might be quite similar to those of the late stages of serpentinization. A caveat of this interpretation is that the different fluid advection velocities in the different seamounts and different extents of seawater entrainment and mixing/precipitation (ie. of aragonite, affecting Sr concentrations) cannot be considered.

South Chamorro's pore water samples document the accumulated trace elements in the fluid present in the subduction channel beneath the mud volcano, mobilized at all temperatures and depths prevailing between trench and conduit. The multiphase serpentinization events observed in the erupted clasts possibly also document the release of serpentinizing fluids at different levels of the decollement: both microfabric observations on the clasts and trace element analyses of the solids erupted by the forearc mud volcanoes indicate a change in the fluid regime. On the one hand, serpentines of the pervasive serpentinization stage and early vein generations formed under low water/rock ratios and are characterized by high trace element contents and Rb/Cs between 1 and 4. In contrast, serpentines in late extensional veins and in the mud formed under higher water/rock ratios, and exhibit still high, but slightly reduced trace element contents with a slightly increased Rb/Cs ratio near 10. Thus, the increasing Rb/Cs ratio observed in successive serpentinization events track the transformation of the compositional pattern of the slab-sourced fluids, being progressively released and accumulated during continued subduction (e.g., Bebout

et al., 2007). In this context, late vein serpentine and mud would represent serpentinization in greater depth nearer to the conduit, while serpentinization of the pervasive stage and the early vein generations might have taken place in shallower parts nearer to the trench. This is consistent with several studies of the Mariana mudflow systems, that have mentioned the possibility that serpentinites formed at shallower levels of the decollement might been carried in deeper parts of the subduction zone, where they would contribute to magma genesis at the arc and backarc regions (Kerrick and Connoly 2001; Savov et al., 2005b, 2007; Snyder et al., 2005; Wei et al., 2005). Thus, clasts and matrix erupted at the mud volcanoes represent a snapshot of these process.

5.4 Generic model for the polyphase serpentinization history of Mariana forearc mantle clasts

The mantle wedge of a cold oceanic subduction zone imposes distinct boundary conditions for fluid migration and mineral-fluid interaction at shallow levels. While the fresh and cold mantle of the tapering wedge would not likely allow mantle convection, the rheology of the serpentinized ultramafic rocks may confine the passage of fluids to fracture bound focused flow, localized around faults or conduits (Fryer, 2012) feeding the serpentine mud volcanoes. Concerning the interaction between mantle and subducting plate, the location of the decoupling-coupling transition (Furukawa, 1993) is of fundamental importance for the advance of serpentinizing reactions in the Mariana forearc mantle. Hyndman and Peacock (2003) propose a thermal structure of a cold oceanic subduction zone (Izu-Bonin), with temperatures in the supra-subduction mantle well below 300 ℃. These authors suggest that a decreased coupling between the subducting plate and mantle wedge is due to serpentinization at the base of the mantle wedge seaward of the arc. Hyndman and Peacock (2003)

furthermore propose that the weak rheology and positive buoyancy of serpentinite will act to isolate hydrated forearc mantle from the overall mantle wedge flow system. By focusing shear deformation in the weak, serpentinized mantle adjacent to the subducting plate, suprasubduction mantle and downgoing slab are mechanically decoupled at the plate interface. This idea is corroborated by findings of simple-shear experiments at a temperature of 200 ℃ and a pressu re of 1.0 GPa (Hirauchi et al., 2010), indicating that the dominant flow mechanism of mesh-textured serpentine (lizardite and chrysotile) evolves with increasing shear strain from inhomogeneous semi-brittle flow to homogeneous ductile flow, rather than faulting, brecciation, or fracturing. Moreover, the confirmation of plastic flow by intracrystalline deformation within individual serpentine grains by Hirauchi et al. (2010) is consistent with textural features observed in highly deformed natural serpentinites (i.e., ribbon texture; Viti and Mellini, 1998; Hirauchi and Yamaguchi, 2007). More recently, deformation experiments on lizardite (in the range of 150-400 °C, 1-8 GPa at varying strain rates) and combined first-principles calculations of Amiguet et al. (2012) revealed strain-rate independent plasticity of lizardite at low stress. Even at the potentially high strain rates prevalent at the shallow mantle wedge (10-20 km depth) of a cold intra-oceanic subduction zone, lizardite is capable of a strain localization into cm-scale shear bands, which provides a plausible mechanism for mobilization of rock fragments in shallower parts of the decollement (Hirauchi et al., 2010).

Two source regions of ultramafic material, mobilized as clasts and erupted in mud flows, seem possible: (i) serpentinization of conduit wall rock and mobilization as clasts in the mud flow, and (ii) clasts of material from the basal plane of the suprasubduction mantle wedge, partly serpentinized and eroded in shallower parts of the decollement. In scenario (i), fluids serpentinizing the conduit wall rocks would derive from the rising mud. The FME-enrichments characteristic of the early phase of serpentinization would imply a temporal change of the FME-contents of these mud

fluids that passing up the conduit, because none of the later generations of serpentinite show this enrichment. Such an oscillation of the degree of FME-enrichment in the mud rising through the conduit systems must have produced likewise clasts with an FME-enrichment pattern reversed to what is actually observed: low-FME concentrations in an early pervasive phase, and high-FME concentrations in late vein stages, and large amounts of high-FME mud serpentine.

However, bulk analyses from clast and mud material (Savov et al., 2005a and 2007) and the analyses of individual serpentine generations in this work uniformly show higher FME in the clast serpentines than in the mud. It is not likely that the mantle rocks forming the conduit walls beneath South Chamorro Seamount first were serpentinized pervasively by fluids emanating from the slab-mantle interface with high-FME concentrations, which then shift to lower FME-concentrations in the later stage of mobilization and massive mud rise. This shift in the trace element signature of the serpentinizing fluid is more plausibly explained by the second scenario outlined above. Mantle material of the basal plane of the suprasubduction mantle wedge is partly serpentinized by fluids derived from the slab sediments in shallower parts of the decollement. These fluids have uniformly high-FME contents which is inherited by the rocks altered during these early serpentinization stages. During descent to the depth of the conduit beneath South Chamorro Seamount, the continued release of fluids from the slab might alter the level of FME-enrichment of the fluid present in the subduction channel that likewise govern the serpentinization of the later clast vein generations and the mud matrix serpentine.

5.5 Summarized microfabric evolution of the polyphase serpentinization of Mariana forearc mantle clasts

Figure 9 presents a schematic view of the relative chronology of the microfabric evolution, summarizing the observed fabric relations of the polyphase serpentinization history of Mariana forearc mantle. The first serpentinization event is believed to have occurred along a discrete set of tiny fractures (mostly < 10 mm) activated by regional brittle deformation (Salisbury et al., 2002), along which formation of magnetite trails can be observed (see Fig. 9A, early magnetite veins). This event was followed by a stage of pervasive serpentinization with low water-rock ratios, which proceeded under a static, isotropic pressure regime, which led to the development of mesh structures and bastitization of orthopyroxene (Fig. 9B). The serpentine formed during this stage (lizardite) has likely been exposed to a relatively unaltered sediment-derived fluid derived from the sedimentary covering the subducting slab, which contained high concentrations of Cs, Rb, Sr and Ba.

The pervasive phase was followed by a phase of the establishment of fluid pathways, generating focused fluid flow along reactivated early magnetite veins, or newly developed type (i) veins, involving occasional isovolumetric metasomatism (SiO_2-loss and halo formation; see Fig. 9C). Metasomatism did not alter the trace element contents present in the serpentine component in Srp-Brc regions. Later serpentinization events document the loss of confining rock pressure and the onset of volumetric expansion (see Fig. 9D) and the shift to higher water-rock ratios, preluding the change from a rock-dominated to a fluid-dominated system: extensional chrysotile veins of type (ii) contain a significant Brc fraction (see Fig. 4C) with intermediate to low Cs and Rb contents, and high Ba and Sr content which are comparable to serpentine of earlier phases. Most probably, the mobilization of wall rock fragments into the mudflow (either in subduction channel or within conduit) involves a transition from a closed system to an open system by development of fluid pathways, similar to the sequence of serpentinization during unroofing of mantle in slow-spreading mid-ocean ridge environments (Andreani et al., 2007).

Further expansion of the rock in the course of continued serpentinization could not be followed by the already completely serpentinized halo at the rim, and this lead to the formation of type (iii) "Frankenstein" veins (see Fig. 9E; Salisbury et al., 2002; see also Iyer et al., 2008b). The serpentine (chrysotile) formed in this phase, and the multiple crack-seal chrysotile veins of type (iv), which document marked anisotropic expansion (see Fig. 9F), exhibit low trace Cs, Rb, Ba, and Sr contents which are comparable to those of bulk mud analyses of Savov et al., (2005), and to spring or pore water compositions of Site 1200. The type (iv) veins we could observe in our samples are located in the rim regions of clast samples 3R-1_3-7, 16R-1_52-54, and 16R-2_7-9. The serpentine formed in both of the later vein generations documents a further change in the serpentinizing fluids, suggesting a diminished influence of solely sediment-derived fluids.

Microfabric information, phase relations (occurrence of the serpentine polymorphs lizardite and chrysotile; presence or absence of brucite) and the correlation of FME-concentrations of the successive serpentinization stages of the Mariana forearc mantle clasts imply some constraints on the nature of the serpentinizing fluids. The absence of brucite in the early serpentinization phase may be explained by the quartz-saturated nature of unaltered sediment-derived fluids. Opal and smectite dehydration produce high-FME (with Rb/Cs < 10; You et al., 1996), quartz-saturated fluids that may initiate early pervasive serpentinization processes at shallow levels. During the continued serpentinization in a still rock-dominated environment, brucite becomes more common, because the high-FME-fluids are either consumed or depleted by early pervasive serpentinization. Eventually, late chrysotile veins (types iii and iv, in which brucite is absent) document the increased access of slab fluids in a now fluid-dominated serpentinization regime. These fluids are still quartz saturated, but geochemical slab signatures in trace elements are lacking, because the

composition of slab-derived fluids has been completely reset by serpentinization reactions and continued diagenetic to metamorphic processes within the subduction channel (Moore and Saffer, 2001). The final stage of diapiric rise of matrix and clasts in the conduits feeding the mud volcanoes is characterized by a very late alteration feature (see Fig. 2H, or also Fig. F78 in Salisbury et al., 2002). Apparently, the "browning" of the clasts from the rim inward (independent of the intra-clast fabric relations) corresponds to re-equilibration with the rising mud fluids that lack buffering by quartz-rich lithologies of the decending slab.

6. Conclusions

Observations on microfabric, petrography and trace element contents of serpentinized ultramafic clasts from South Chamorro Seamount provide novel insights into the prevailing conditions in the shallow mantle beneath the Mariana forearc. Detailed analyses of phase relations (low-temperature serpentine polymorphs lizardite and chrysotile, absence of antigorite and magnetite) and mineral chemistry of the successive serpentine generations present in the clasts, as well as oxygen isotope data, reveal low-temperature conditions ($\leq$ 250 ℃), as proposed by thermal models of cold oceanic subduction zones. Correlation of trace element concentrations and ratios in serpentine from clasts and mud matrix with either mud-volcano pore water analyses or experimental investigations of trace element mobilization reveal fluids derived from sediments at low temperatures as potential source of the serpentinizing fluids.

The rheological properties of suprasubduction mantle material in a cold oceanic subduction zone pose distinct boundary conditions on the serpentinization

processes: (i) convection is absent in the tapering mantle wedge above the decoupling-coupling transition; (ii) within the wedge, and likely on the interface between subducting slab and overlying mantle, lizardite is capable of a strain localization into sample-scale shear bands. Therefore, within the wedge, the passage of fluids may be confined to fractures, which is the prerequisite for the transfer of serpentinized bouyant material to rise from the slab-mantle interface via conduits to the mounds of the mud volcanoes. Moreover, due to the characteristic mechanical properties of the low-temperature serpentine phases, partly serpentinized mantle material can be eroded at shallow levels of the decollement from the basal interface downward in the subduction channel, and still preserve fabric records and chemical signatures of the early stages of serpentinization.

High concentrations of fluid mobile elements in the early stages of the polyphase serpentinization history of the clasts, in contrast to FME-poor serpentine present in the late vein generations in these clasts and also in the mud matrix serpentine point to a change in the nature of the serpentinizing fluids throughout the history of serpentinization and eruption. We propose, that the continued microfabric and mineral chemical evolution observed in the ultramafic clasts is consistent with (1) the partial serpentinization and erosion of mantle material off the basal plane of the suprasubduction mantle wedge in shallower parts of the decollement, (2) the subsequent descent in the subduction channel to the depth beneath South Chamorro Seamount, and (3) the rise as clasts through the conduit towards the mound of the mud volcano.

Sediments seem to play a vital role not only in the explanation of the observed trace element ratios in the actual samples, but potentially also for the generation of fluids under low-T conditions, and thus promoting the formation of mud volcanos in forearc regions of nonaccretionary cold subduction zones. With this respect, additional

experimental data on the mobilization of FME from sediments are essential, especially on the partition coefficients of these with the different serpentine polymorphs. Moreover, research on the occurrence of certain serpentine polymorphs in different serpentinization microfabrics may allow for more detailed mass (and volume) balanced estimations. This will further the understanding of how subduction-zone processes are connected to the hydration of ultramafic rocks.

Acknowledgements

We thank Barbara Mader and Peter Appel for assistance with the electron microprobe, Andreas Klügel for help with the LA-ICP-MS analyses, Christoph Vogt for performing the XRD measurements. Many thanks go to Håkon Austrheim, Kartik Iyer, Oliver Plümper, and Tim Schroeder for inspiring and stimulating discussions. NJ and WB acknowledge support through Research Center/Excellence Cluster 'The Ocean in the Earth System'. This study was funded through a grant of the DFG to WB (BA 1605/5-1).

References

Alt, J.C., Shanks III, W.C., 2006. Stable isotope compositions of serpentinite seamounts in the Mariana forearc: serpentinization processes, fluid sources and sulphur metasomatism. Earth and Planetary Science Letters 242, 272-285.

Alt, J. C., Laverne, C., Coggon, R.M., Teagle, D.A.H., Banerjee, N.R., Morgan, S., Smith‐Duque, C.E., Harris, M., Galli, L., 2010. Subsurface structure of a submarine

hydrothermal system in ocean crust formed at the East Pacific Rise, ODP/IODP Site 1256. Geochemistry, Geophysics, Geosystems 11, Q10010.

Andreani, M., Baronnet, A., Boullier, A.-M., Gratier, J.-P., 2004. A microstructural study of a crack-seal type serpentine vein, using SEM and TEM techniques. European Journal of Mineralogy 16, 585-595.

Andreani, M., Mével, C., Boullier, A.-M., Escartin, J., 2007. Dynamic control on serpentine crystallization in veins: constraints on hydration processes in oceanic peridotites. Geochemistry, Geophysics, Geosystems 8, Q02012.

Andreani, M., Muñoz, M., Marcaillou, C., Delacour, A., 2013. μXANES study of iron redox state in serpentine during oceanic serpentinization. Lithos 178, 70-83.

Armstrong, J.T., 1995. CITZAF: A package of correction programs for the quantitative electron microbeam X-ray analysis of thick polished materials, thin films, and particles. Microbeam Analysis 4, 177-200.

Auzende, A.-L., Daniel, I., Reynard, B., Lemaire, C., Guyot, F., 2004. High-pressure behaviour of serpentine minerals: a Raman spectroscopic study. Physics and Chemistry of Minerals 31, 269-277.

Bach, W., Paulick, H., Garrido, C. J., Ildefonse, B., Meurer, W.P., and Humphris, S. E., 2006. Unraveling the sequence of serpentinitzation reactions: petrography, mineral chemistry, and petrophyscis of serpentinites from MAR 15ºN (ODP Leg 209, Site 1274). Geophysical Research Letters 33, L13306.

Beard, J.S., Frost, B.R., Fryer, P., McCaig, A., Searle, R., Ildefonse, B., Zinin, P., Sharma, S.K., 2009. Onset and progression of serpentinization and magnetite formation in olivine-rich troctolite from IODP Hole U1309D. Journal of Petrology 50, 387-403.

Bebout, G.E., Bebout, A.E., Graham, C.M., 2007. Cycling of B, Li, and LILE (K, Cs, Rb, Ba, Sr) into subduction zones: SIMS evidence from micas in high-P/T metasedimentary rocks. Chemical Geology 239, 284-304.

Bebout, G.E., 2007. Metamorphic chemical geodynamics of subduction zones. Earth and Planetary Science Letters 260, 373-393.

Becker, J.J., Sandwell, D.T., Smith, W.H.F., Braud, J., Binder, B., Depner, J., Fabre, D., Factor, J., Ingalls, S., Kim, S.-H., Ladner, R., Marks, K., Nelson, S., Pharaoh, A., Trimmer, R., von Rosenberg, J., Wallace, G., Weatherall, P., 2009. Global bathymetry and elevation data at 30 Arc seconds resolution: SRTM30_PLUS. Marine Geodesy 32, 355-371.

Benton, L.D., Ryan J.G., Tera, F., 2001. Boron isotope systematics of slab fluids as inferred from a serpentine seamount, Mariana forearc. Earth and Planetary Science Letters 187, 273-82.

Bloomer, S.H., 1983. Distribution and origin of igneous rocks from the landward slopes of the Mariana Trench: implications for its structure and evolution. Journal of Geophysical Research 88, 7411-28.

Bonatti, E., Michael, P.J., 1989. Mantle peridotites from continental rifts to ocean basins to subduction zones. Earth and Planetary Science Letters 91, 297-311.

Bons, P.D., Elburg, M.A., Gomez-Rivas, E., 2012. A review of the formation of tectonic veins and their microstructures. Journal of Structural Geology 43, 33-62.

Boudier, F., Baronnet, A., Mainprice, D., 2010. Serpentine mineral replacements of natural olivine and their seismic implications: Oceanic lizardite versus subduction-related antigorite. Journal of Petrology 51, 495-512.

Clayton, R.N., Mayeda, T.K., 1963. The use of bromine pentafluoride in the extraction of oxygen from oxides and silicates for isotopic analysis. Geochimica Cosmochimica Acta 27, 43-52.

Cloos, M., Shreve, R.L., 1988a. Subduction-channel model of prism accretion, melange formation, sediment subduction, and subduction erosion at convergent plate margins; Part I, background and description. Pure and Applied Geophysics 128, 455-500.

Cloos, M., Shreve, R.L., 1988b. Subduction-channel model of prism accretion, melange formation, sediment subduction, and subduction erosion at convergent plate margins; Part II, implications and discussion. Pure and Applied Geophysics 128, 501-545.

D'Antonio, M., Kristensen, M.B., 2004. Serpentine and brucite of ultramafic clasts from the South Chamorro Seamount (Ocean Drilling Program Leg 195, Site 1200): Inferences for the serpentinization of the Mariana forearc mantle. Mineralogical Magazine 68, 887-904.

Deschamps, F., Guillot, S., Godard, M., Chauvel, C., Andreani, M., Hattori, K., 2010. In situ characterization of serpentinites from forearc mantle wedges: timing of serpentinization and behavior of fluid-mobile elements in subduction zones. Chemical Geology 269, 262-277.

Deschamps, F., Guillot, S., Godard, M., Andreani, M., Hattori, K., 2011. Serpentinites act as sponges for fluid-mobile elements in abyssal and subduction zone environments. Terra Nova 23, 171-178.

Dilek, Y., Coulton, A.J., Hurst, S.D., 1997. Serpentinization and hydrothermal veining in peridotites at site 920 in the Mark area. Proceedings of the Ocean Drilling Program, Scientific Results 153, pp. 35-59.

Escartín, J., Hirth, G., B. Evans, B., 1997. Effects of serpentinization on the lithospheric strength and the style of normal faulting at slow-spreading ridges. Earth and Planetary Science Letters 151, 181-189.

Evans, B.W., 2004. The serpentine multisystem revisited: chrysotile is metastable. International Geology Review, 46, 479-506.

Fryer, P., 1992. A synthesis of Leg 125 drilling of serpentine seamounts on the Mariana and Izu-Bonin forearcs. In: Dearmont, L.H., Mazzullo, E.K., Stewart, N.J., Winkler, W.R., (Eds.), Proceedings of the Ocean Drilling Program, Scientific Results, 125, pp. 593-614.

Fryer, P., 1996. Evolution of the Mariana Convergent Plate Margin System. Reviews of Geophysics 34(1), 89-125.

Fryer, P., Ambos, E.L., Hussong, D.M., 1985. Origin and emplacement of Mariana forearc seamounts. Geology 13, 774-777.

Fryer, P., Fryer, G.J., 1987. Origin of non-volcanic seamounts in a forearc environment. Seamounts, Islands and Atolls: In: Keating, B., Fryer, P., Batiza, R. (Eds.), A.G.U. Geophysical Monograph, 43, pp. 61-69.

Fryer, P., Pearce, Julian A., Stokking, Laura B., et al., 1990. Bonin/Mariana region, covering Leg 125 of the cruises of the drilling vessel JOIDES Resolution, Apra Harbor, Guam, to Tokyo, Japan, sites 778–786. In: Fryer, P., Pearce, J.A., Stokking, L.B., et al. (Eds.), Proceedings of the Ocean Drilling Program Initial Reports, 125, pp. 367-380.

Fryer, P., Wheat, C.G., Mottl, M.J., 1999. Mariana Blueschist mud volcanism: implications for conditions within the subduction zone. Geology 27, 103-106.

Fryer, P., Lockwood, J., Becker, N., Todd, C., Phipps, S., 2000. Significance of serpen- tine and blueschist mud volcanism in convergent margin settings. In: Dilek, Y., et al. (Ed.), Ophiolites and Oceanic Crust: New Insights from Field Studies and Ocean Drilling Program: Special Papers Geological Society of America, 349, pp. 35-51.

Fryer, P., Salisbury, M.H., 2006. Leg 195 synthesis: site 1200 - serpentinite seamounts of the Izu Bonin/Mariana convergent plate margin (ODP Leg 125 and 195 drilling results). In: Shinohara, M., Salisbury, M.H., Richter, C. (Eds.), Proceedings of the Ocean Drilling Program, Scientific Results, 195, pp. 1-30.

Furukawa, Y., 1993. Depth of the decoupling plate interface and thermal structure under arcs. Journal of Geophysical Research 98, 20,005-20,013.

Godard, M., Luquot, L., Andreani, M., Gouze, P., 2013. Incipient hydration of mantle lithosphere at ridges: A reactive-percolation experiment. Earth and Planetary Science Letters 371-372, 92-102.

Groppo, C., Rinaudo, C., Cairo, S., Gastaldi, D., Compagnoni, R., 2006. Micro-Raman spectroscopy for a quick and reliable identification of serpentine minerals from ultramafics. European Journal of Mineralogy 18, 319-329.

Hirauchi, K., Katayama, I., Uehara, S., Miyahara, M., Takai, Y., 2010. Inhabitation of subduction thrust earthquakes by low-temperature plastic flow in serpentine. Earth and Planetary Science Letters 295, 349-357.

Hulme, S., Wheat, C.G., Fryer, P., Mottl, M.J., 2010. Pore-water chemistry of the Mariana serpentinite mud volcanoes: a window to the seismogenic zone. Geochemistry, Geophysics, Geosystems 11, Q01X09.

Hyndman, R.D., Peacock, S.M., 2003. Serpentinization of the forearc mantle. Earth and Planetary Science Letters 212, 417-432.

Ishii, T., Robinson, P.T., Maekawa, H., Fiske, R., 1992. Petrological studies of peridotites from diapiric serpentinite seamounts in the Izu-Ogasawara-Mariana forearc, Leg 125. In: Fryer, P., Pearce, J.A., Stokking, L.B., et al. (Eds.), Proceedings of the Ocean Drilling Program, Scientific Results, 125, pp. 445-485.

Iyer, K., Austrheim, H., John, T., Jamtveit, B., 2008a. Serpentinization of the oceanic lithosphere and some geochemical consequences: constraints from the Leka Ophiolite complex, Norway. Chemical Geology 249(1-2), 66-90.

Iyer, K., Jamtveit, B., Mathiesen, J., Malthe-Sorenssen, A., Feder, J., 2008b. Reaction-assisted hierarchical fracturing during serpentinization. Earth and Planetary Science Letters 267(3-4), 503-516.

Jochum, K. P., Weis, U., Stoll, B., Kuzmin, D., Yang, Q., Raczek, I., Jacob, D. E., Stracke, A., Birbaum, K., Frick, D. A., Günther, D., Enzweiler, J., 2011. Determination of Reference Values for NIST SRM 610-617 Glasses Following ISO Guidelines. Geostandards and Geoanalytical Research 35, 397-429.

Jochum, K.P., Stoll, B., Herwig, K., Willbold, M., Hofmann, A.W., Amini, M., Aarburg, S., Abouchami, W., Hellebrand, E., Mocek, B., Raczek, I., Stracke, A., Alard, O., Bouman, C., Becker, S., Dücking, M., Brätz, H., Klemd, R., de Bruin, D., Canil, D., Cornell, D., de Hoog, C.-J., Dalpé, C., Danyushevsky, L., Eisenhauer, A., Gao, Y., Snow, J.E., Groschopf, N., Günther, D., Latkoczy, C., Guillong, M., Hauri, E.H., Höfer, H.E., Lahaye, Y., Horz, K., Jacob, D.E., Kasemann, S.A., Kent, A.J.R., Ludwig, T., Zack, T., Mason, P.R.D., Meixner, A., Rosner, M., Misawa, K., Nash, B.P., Pfänder, J., Premo, W.R., Sun, W.D., Tiepolo, M., Vannucci, R., Vennemann, T., Wayne, D., Woodhead, J.D., 2006. MPI-DING reference glasses for in situ microanalysis: new reference values for element concentrations and isotope ratios. Geochemistry, Geophysics, Geosystems 7, Q02008.

Katayama, I., 2009. Thin anisotropic layer in the mantle wedge beneath northeast Japan. Geology 37, 211-214.

Klein, F., Bach, W., Jöns, N., McCollom, T., Moskowitz, B., Berquó, T., 2009. Iron partitioning and hydrogen generation during serpentinization of abyssal peridotites from 15°N on the Mid-Atlantic Ridge. Geochimica et Cosmochimica Acta 73, 6868-6893.

Klein, F., Bach, W., Humphris, S. E., Kahl, W.-A., Jöns, N., Moskowitz, B., Berquó, T., 2014. Magnetite in seafloor serpentinite - Some like it hot. Geology 42(2), 135-138.

Kodolanyi, J., Pettke, T., Spandler, C., Kamber, B.S., Gmeling, K., 2012. Geochemistry of ocean floor and fore-arc serpentinites: Constraints on the ultramafic input to subduction zones. Journal of Petrology 53, 235-270.

Lafay, R., Montes-Hernandez, G., Janots, E., Chiriac, R., Findling, N., Toche, F., 2012. Mineral replacement rate of olivine by chrysotile and brucite under high alkaline conditions. Journal of Crystal Growth 347, 62-72.

Lawrence, J.R., Drever, J.L., 1981. Evidence for cold water circulation at DSDP Site 395: isotopes and chemistry of alteration products. Journal of Geophysical Research 86, 5125-5133.

Meffre, S., Falloon, T.J., Crawford, T.J., Hoernle, K., Hauff, F., Duncan, R.A., Bloomer, S.H., Wright, D.J., 2012. Basalts erupted along the Tongan fore arc during subduction initiation: Evidence from geochronology of dredged rocks from the Tonga fore arc and trench. Geochemistry, Geophysics, Geosystems 13, Q12003.

Mellini, M., Rumori, C., Viti, C., 2005. Hydrothermally reset magmatic spinels in retrograde serpentinites, formation of “ferritchromit” rims and chlorite aureoles. Contributions to Mineralogy and Petrology 149, 266-275.

Michibayashi, K., Tasaka, M., Ohara, Y., Ishii, T., Okamoto, A., Fryer, P., 2007. Variable microstructure of peridotite samples from the southern Mariana Trench: evidence of a complex tectonic evolution. Tectonophysics 444, 111-118.

Moore, J.C., Saffer, D., 2001. Updip limit of the seismogenic zone beneath the accretionary prism of southwest Japan: An effect of diagenetic to low-grade metamorphic processes and increasing effective stress. Geology 29(2), 183–186.

Mottl, M.J., 1992. Pore waters from serpentine seamounts in the Mariana and Izu-Bonin forearcs, Leg 125: evidence for volatiles from the subducting slab. In: Fryer, P., Pearce, J.A., Stokking, L.B., et al. (Eds.), Proceedings of the Ocean Drilling Program, Scientific Results, 125, pp. 373-385.

Mottl, M.J., Komor, S.C., Fryer, P. Moyer, C.L., 2003. Deep-slab fluids fuel extremophilic Archaea on a Mariana forearc serpentinite mud volcano: Ocean Drilling Program Leg 195. Geochemistry Geophysics and Geosystems 4(11), 9009.

Mottl, M.J., Wheat, C.G., Fryer, P., Gharib, J., Martin, J.B., 2004. Chemistry of springs across the Mariana forearc shows progressive devolatilization of the subducting plate. Geochimica et Cosmochimica Acta 68(23), 4915-4933.

Murata, K., Maekawa, H., Yokose, H., Yamamoto, K., Fujioka, K., Ishii, T., Chiba, H., Wada, Y., 2009. Significance of serpentinization of wedge mantle peridotites beneath Mariana forearc, western Pacific. Geosphere, 5, 90-104.

Oakley, A.J., Taylor, B., Fryer, P., Moore, G.F., Goodliffe, A.M., Morgan, J.K., 2007. Emplacement, growth, and gravitational deformation of serpentinite seamounts on the Mariana forearc, Geophysical Journal International 170(2), 615-634.

O'Hanley, D.S. (1996) Serpentinites: Record of Tectonic and Petrologic History. New York: Oxford University Press.

Pabst, S., Zack, T., Savov, I.P., Ludwig, T., Rost, D., Vicenzi, E.P., 2011. Evidence for boron incorporation into the serpentine crystal structure. American Mineralogist, 96, 1112-1119.

Pabst, S., 2009. Investigation of blueschist and serpentinized harzburgite from the Mariana forearc: Insights into the mechanisms of element mobilization in subduction zones and storage of fluid-mobile elements in the mantle wedge. PhD Dissertation, Heidelberg, Germany. http://www.ub.uni-heidelberg.de/archiv/10181.

Parkinson, I.J., Pearce, J.A., 1998. Peridotites from the Izu-Bonin-Mariana forearc (ODP Leg 125), Evidence for mantle melting and melt-mantle interaction in a supra-subduction zone setting. Journal of Petrology 39, 1577-1618.

Pearce, J.A., Baker, P.F., Edwards, S.J., Parkinson, I.J., Leat, P.T., 2000. Geochemistry and tectonic significance of peridotites from the South-Sandwich arc-basin system, South Atlantic. Contributions to Mineralogy and Petrology 139, 36-53.

Plank, T., Langmuir, C., 1998. The chemical composition of subducting sediment and its consequences for the crust and mantle. Chemical Geology 145, 325-394.

Plümper, O., Røyne, A., Magrasó, A., Jamtveit, B., 2012. The interface-scale mechanism of reaction-induced fracturing during serpentinization. Geology 40, 1103-1106.

Reynard, B., 2013. Serpentine in active subduction zones. Lithos 178, 15, 171-185.

Rinaudo, C., Gastaldi, D., Belluso, E., 2003. Characterization of chrysotile, antigorite and lizardite by FT-Raman spectroscopy. Canadian Mineralogist 41, 883-890.

Rüpke, L.H., Morgan, J.P., Hort, M., Connolly, J.A.D., 2002. Are the regional variations in Central American arc lavas due to differing basaltic versus peridotitic slab sources of fluids? Geology 30, 1035-1038.

Rüpke, L.H., Morgan, J.P., Hort, M., Connolly, J.A.D., 2004. Serpentine and the subduction zone water cycle. Earth and Planetary Science Letters 223, 17-34.

Sakai, R., Kusakabe, M., Noto, M., Ishii, T., 1990. Origin of waters responsible for serpentinization of the Izu-Ogasawara-Mariana forearc seamounts in view of hydrogen and oxygen isotope ratios. Earth and Planetary Science Letters 100(1-3), 291-303.

Saboda, K.L., Fryer, P., Maekawa, H., 1992. Metamorphism of ultramafic clasts from Conical Seamount: sites 778, 779, and 780. In: Fryer, P., Pearce, J.A., Stokking, L.B., et al. (Eds.), Proceedings of the Ocean Drilling Program, Scientific Results, 125, pp. 373-385. pp. 431-444.

Salisbury, M.H., Shinohara, M., Richter, C., Araki, E., Barr, S.R., D'Antonio, M., Dean, S.M., Diekmann, B., Edwards, K.M., Fryer, P.B., Gaillot, P.J., Hammon III,

W.S., Hart, D., Januszczak, N., Komor, S.C., Kristensen, M.B., Lockwood, J.P., Mottl, M.J., Moyer, C.L., Nakahigashi, K., Savov, I.P., Su, X., Wei, K.-Y., Yamada, T., 2002. Proceeding of the Ocean Drilling Program, Initial Reports, 195.

Saumur, B.M., Hattori, K., 2013. Zoned Cr-spinel and ferritchromite alteration in forearc mantle serpentinites of the Rio San Juan Complex, Dominican Republic. Mineralogical Magazine 77 (1), 117–136.

Savov, I.P., Guggino, S., Ryan, J.G., Fryer, P., Mottl, M.J., 2005a. Geochemistry of serpentinite muds and metamorphic rocks from the Mariana forearc, ODP Sites 1200 and 778–779, South Chamorro and Conical Seamounts. In: Shinohara, M., Salisbury, M.H., Richter, C. (Eds.), Proceedings of the Ocean Drilling Program, Scientific Results, 195.

Savov, I.P., Ryan, J.G., D'Antonio, M., Kelley, K., Mattie, P., 2005b. Geochemistry of ser- pentinized peridotites from the Mariana Forearc Conical Seamount, ODP Leg 125: Implications for the elemental recycling at subduction zones. Geochemistry, Geophysics, Geosystems 6.

Savov, I.P., Ryan, J.G., D'Antonio, M., Fryer, P., 2007. Shallow slab fluid release across and along the Mariana arc-basin system: Insights from geochemistry of serpentinized peridotites from the Mariana fore arc. Journal of Geophysical Research-Solid Earth 112, B09205.

Schmidt, M.W., Poli, S., 1998. Experimentally based water budgets for dehydrating slabs and consequences for arc magma generation. Earth and Planetary Science Letters 163, 361-379.

Schwartz, S., Guillot, S., Reynard, B., Lafay, R., Debret, B., Nicollet, C., Lanari, P., Auzende, A. L., 2012. Pressure-temperature estimates of the lizardite/antigorite transition in high pressure serpentinites. Lithos 178, 197-210.

Seyfried, W.E.,Jr., Foustoukos, D.I., Fu, Q., 2007. Redox evolution and mass transfer during serpentinization: An experimental and theoretical study at 200℃, 500 bar with implications for ultramafic-hosted hydrothermal systems at Mid-Ocean Ridges. Geochimica et Cosmochimica Acta 71, 3872-3886.

Seyler, M., Toplis, M.J., Lorand, J.P., Luguet, A., Cannat, M., 2001. Clinopyroxene microtextures reveal incompletly extracted melts in abyssal peridotites. Geology 29, 155-158.

Snyder, G.T., Savov, I.P., Muramatsu, Y., 2005. Iodine and boron in Mariana serpentinite mud volcanoes (ODP Legs 125 and 195): implications for forearc processes and subduction recycling. In: Shinohara, M., Salisbury, M.H., Richter, C. (Eds.), Proceedings of the Ocean Drilling Program, Scientific Results, 195.

Spandler, C., Pirard, C., 2013. Element recycling from subducting slabs to arc crust: A review. Lithos 170-171, 208-223.

Straub, S.M., Layne, G.D., 2003. Decoupling of fluids and fluid-mobile elements during shallow subduction: evidence from halogen-rich andesite melt inclusions from the Izu arc volcanic front. Geochemistry, Geophysics, Geosystems 4.

Tibi, R., Wiens, D.A., Yuan, X., 2008. Seismic evidence for widespread serpentinized forearc mantle along the Mariana convergence margin. Geophysical Research Letters 35, L13303.

Wheat, C.G., Fryer, P., Fisher, A.T., Hulme, S., Jannasch, H., Mottl, M.J., Becker, K., 2008. Borehole observations of fluid flow from South Chamorro Seamount, an active serpentinite mud volcano in the Mariana forearc. Earth and Planetary Science Letters 267, 401-409.

Wicks, F.J., Whittaker, E.J.W., 1977. Serpentine texture and serpentinization. Canadian Mineralogist 15, 459-488.

Wei, W., Kastner, M., Deyhle, A., Spivack, A.J., 2005. Geochemical cycling of fluorine, chlorine, bromine, and boron and implications for fluid-rock reactions in Mariana forearc, South Chamorro Seamount, ODP Leg 195. In: Shinohara, M., Salisbury, M. H., Richter, C. (Eds.), Proceedings of the Ocean Drilling Program, Scientific Results, 195.

You, C.-F., Castillo, P.R., Gieskes, J.M., Chan, L.H., Spivack, A.J., 1996. Trace element behavior in hydrothermal experiments: implications for fluid processes at shallow depths in subduction zones. Earth and Planetary Science Letters 140, 41-52.

Figure Captions

Fig. 1

(A) Bathymetric map of the Mariana arc-basin system showing the location of South Chamorro Seamount, 85 km from the trench (Leg 195, Site 1200A). Regional map prepared using GMT (Wessel and Smith, 1991). Elevation data from the SRTM30_PLUS dataset (Becker et al., 2009). (B) Schematic diagram (no vertical exaggeration) of the emplacement of serpentinite mud volcanoes on the outer Mariana Forearc (modified from Oakley et al., 2007). The asterisk marks the relative position of South Chamorro Seamount.

Fig. 2

Thin section photomicrographs of serpentinized ultramafic clasts documenting the polyphase serpentinization history of the Mariana forearc mantle. (A) Sample 12R-1, 8-11 cm, showing early magnetite-bearing veins predating the pervasive stage, developed linearly without marked conformance with the rock fabric. Back-scattered electron image. (B) Expansional chrysotile type (ii) veins (brown) in sample 16R-2, 11-12 cm. Scanned thin section, plane-polarized light, image width 16 mm. (C) Close-up of type (ii) veins in sample 16R-2, 7-9 cm, crossing pervasively serpentinized harzburgite with relict olivine subgrains. Photomicrograph, cross-polarized light, image width 1.7 mm. (D1 and D2) Type (iii) veins ("Frankenstein veins"), developed in the halo of type (i) veins and crosscutting type (ii) veins in sample 7R-2, 40-43 cm. Scanned thin section, plane- and cross-polarized, respectively Image width D1 is 11 mm. (E) Type (iii) veins in the halo of type (i) veins in sample 13R-2, 5-7 cm. Scanned thin section, cross-polarized light. Image height 10 mm. (F) Late-stage type (iv) veins of the multiple crack-seal type, indicating clearly anisotropic expansion in sample 3R-1, 3-7 cm. Scanned thin section, plane-polarized light, image width 10.5 mm. (G) Dunite sample 9R-1, 21-23 cm. Ribbons contain submicroscopic intergrowth of serpentine and brucite. On the contrary, large,

recrystallized brucite is observed in regions separated by the ribbons. Image height 2.2 mm. (H) Samples 16R-1, 52-54 cm, and 16R-1, 62-64 cm, both from piece 11A, show browning, occuring from the clast's rim inward, which involves brucite formation in interstices. Scanned thin section, plane-polarized light. Image width 8 mm.

Fig. 3

Detailed view of pervasive serpentinization fabrics. (A) and (B) Sample 7R-2, 40-43 cm. Mesh textures developed in the forearc setting lack the formation of magnetite along mesh rims. Instead, awaruite and submicroscopic intergrowth of brucite and serpentine is observed. (C) and (D) Qualitative analyses of the same sample, indicating the absence of brucite rims around olivine cores.

Fig. 4

Compositions of primary and secondary minerals of the different serpentinization events, plotted as molar proportions of Si-Mg-Fe in ternary diagrams. Primary minerals are given for orientation, they are not part of the assemblage. (A1) and (A2) Serpentine analyses of the pervasive stage in harzburgites and dunites. In dunites, the analyses low in Si are from recrystallized hourglass textures. (B) Analyses of serpentine-brucite phases from type (i) veins and the adjacent halo region. (C) Composition of serpentine-brucite, submicroscopically intergrown in expansional type (ii) veins in harzburgite. (D) Serpentine analyses of type (iii) and type (iv) veins, indicating anisotropic expansion in the course of the serpentinization process.

Fig. 5

Variations of SiO_2, Al_2O_3, CaO and Cr_2O_3 content in primary and secondary minerals. (A) SiO_2 wt.% vs. Al_2O_3 wt.%. Serpentine grown after pyroxene shows Al_2O_3 as high as the precursor mineral, whereas serpentine grown in later events or after olivine shows low to intermediate Al contents. (B) In terms of CaO, bastites show similar

contents as orthopyroxene. On the contrary, serpentine grown from olivine or during later events is enriched in Ca relative to olivine. (C) Cr_2O_3 content of bastites overlap with pyroxene Cr contents, whereas serpentine formed from olivine or during later events contains as low Cr as the primary olivine.

Fig. 6

Trace element (Ni, V) - Si/(Mg+Fe) relationships in primary and secondary minerals. (A) Ni concentrations detected in serpentine-brucite intergrowth regions positively correlate with the serpentine fraction in the mixed analyses. (B) V is neither found in serpentine-brucite intergrowth regions, nor in type (ii) veins. (C) The Ni-V variation diagram shows the discriminatory significance for identifying the serpentine precursor mineral.

Fig. 7

Concentrations of B, Ba, Sr, Rb, and Cs in serpentine and serpentine-brucite mixed analyses. (A) to (E) Boron contents in general increase with increasing Srp-fraction in the mixed Srp-Brc analyses, showing medium to high B values both for early and late vein generations. Barium and Sr show high contents also in the type (ii) veins, but not in type (iii) and type (iv) late-stage veins. Cs and Rb exhibit marked enrichment in early serpentinization stages, and low contents in all types of late extensional veins. (F) Boron-Cs variation diagram, showing the overall high B contents of the serpentinization fluids of the various stages, in comparison to Cs in Srp, which exhibits markedly different concentrations throughout the serpentinization history.

Fig. 8

Diagrams of (A) Cs vs. Rb, and (B) Sr vs. Ba in primary minerals and serpentine of the various serpentine generations. In both diagrams, fields of bulk rock analyses of

1200A clasts and mud from Savov et al., (2007, and 2005a) are given. For comparison, Cs and Rb contents of forearc peridotites (Meffré et al., 2012), altered oceanic crust (Kelley et al., 2006), and of sediments (Plank and Langmuir, 1998) are shown. Furthermore, compositions of natural (Mottl et al., 2004) and experimental fluids and solids (Y-You et al., 1996) are plotted. See text for further discussion.

Fig. 9

Relative chronology of the microfabric evolution, summarizing the observed fabric relations and generalized trace element concentrations of the polyphase serpentinization history of Mariana forearc mantle. (A) First serpentinization event along a discrete set of tiny fractures. (B) Phase of pervasive serpentinization under a static, isotropic pressure regime. (C) Phase of establishment of fluid pathways, generating focused fluid flow along type (i) veins. (D) Onset of anisotropic expansion features and occurrence of extensional type (ii) veins. (E) Formation of type (iii) veins in outer rock/clast (?) halo regions of type (i) veins to compensate continued expansion of the inner parts. (F) Multiple crack-seal veins of type (iv), located in the rim regions of the clasts.

Tables

Table 1.

Samples (clasts) from South Chamorro Smt., Leg 195, Site 1200A.

Table 2.

Representative electron microprobe analyses and in situ LA-ICP-MS data of relict primary minerals from Leg 195, Site 1200A, South Chamorro Smt.

Table 3.

Representative electron microprobe analyses and in situ LA-ICP-MS data of serpentinization products from Leg 195, Site 1200A, South Chamorro Smt.

Table 4.

Overview of selected properties of serpentine from different serpentinization events.

Table 5.

Oxygen isotope data of serpentinization products from different serpentinization phases in ultramafic clasts from South Chamorro Smt., Leg 195, Site 1200A.

Figure1
Click here to download high resolution image

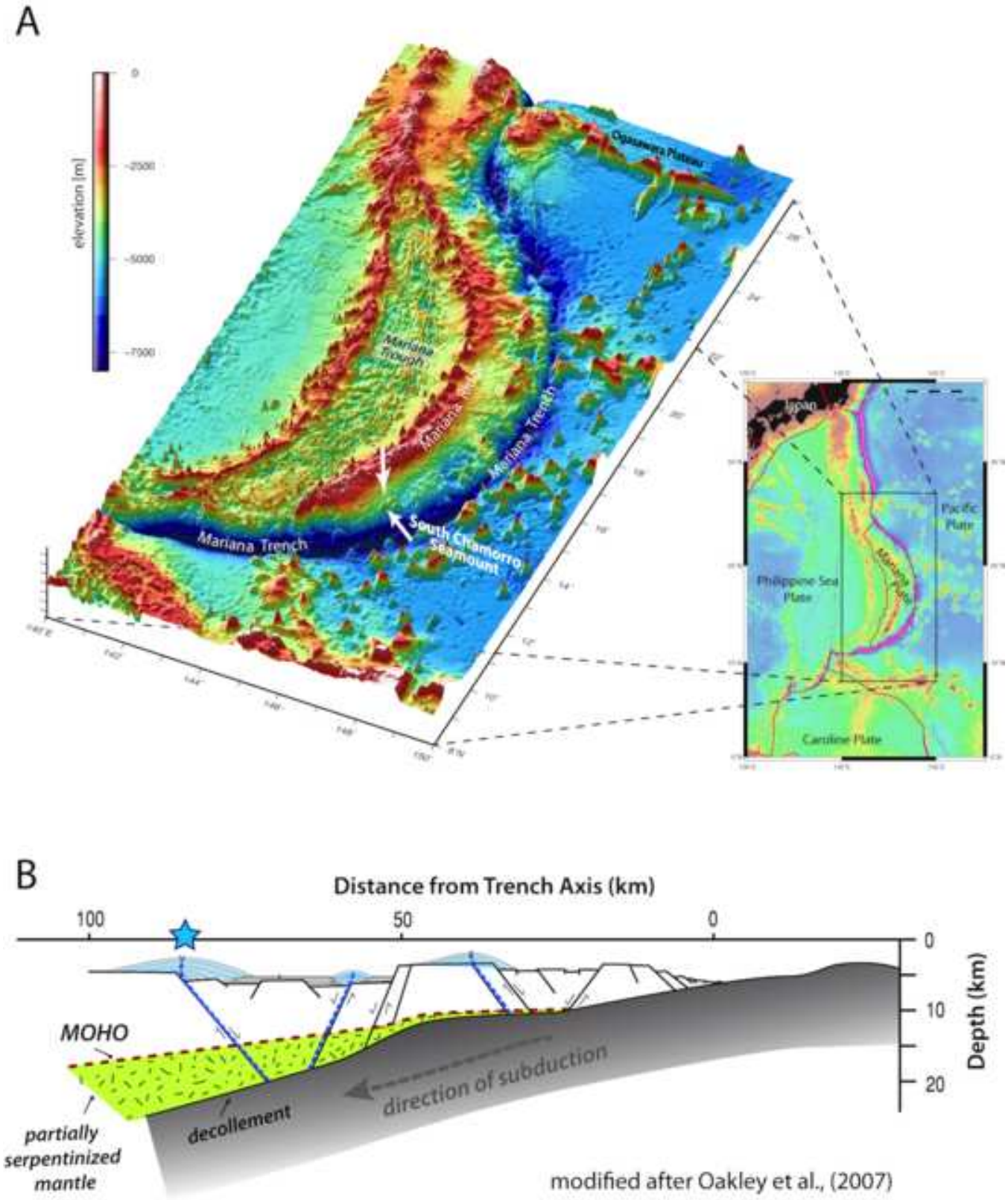

Figure2

Click here to download high resolution image

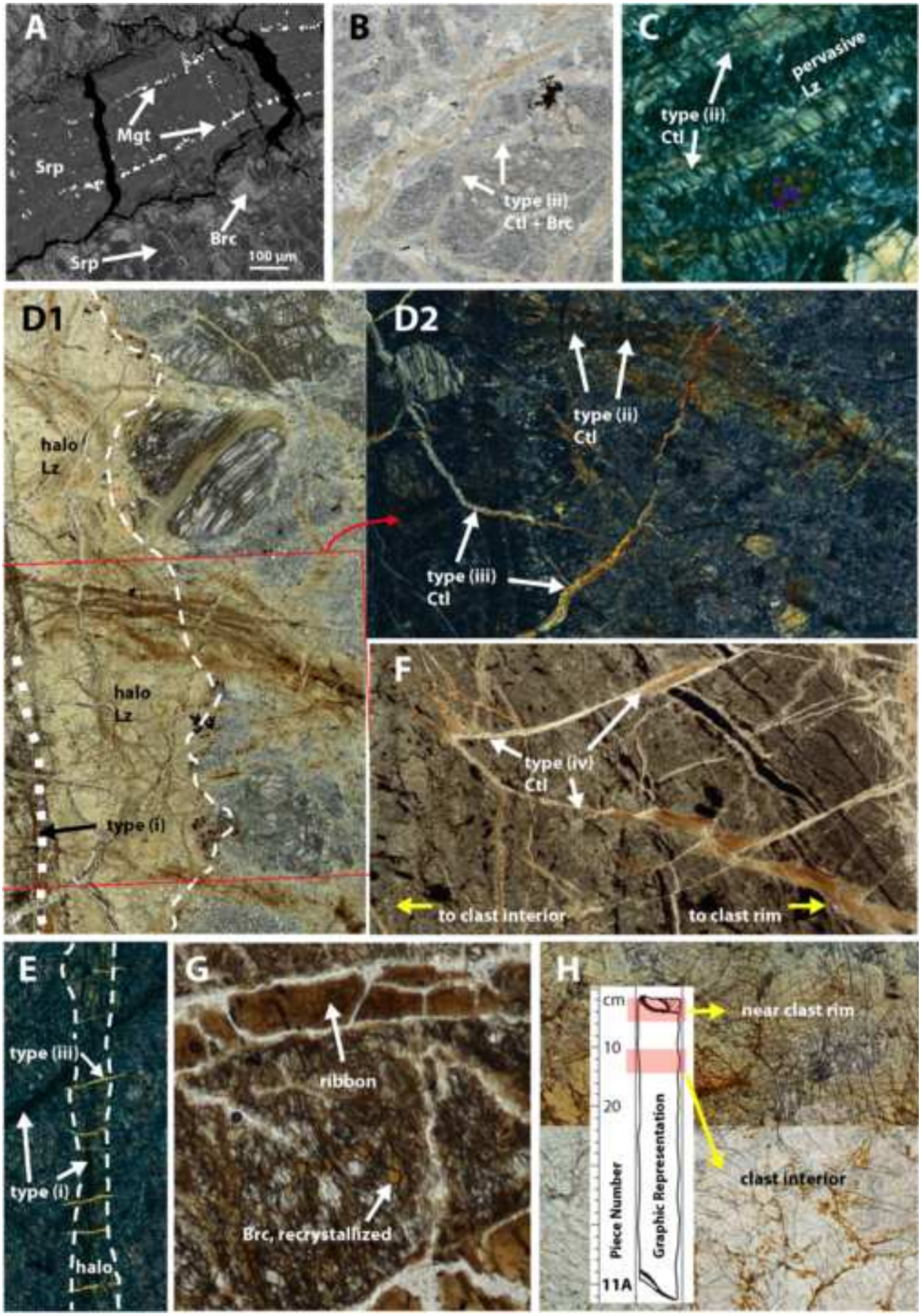

Figure3
Click here to download high resolution image

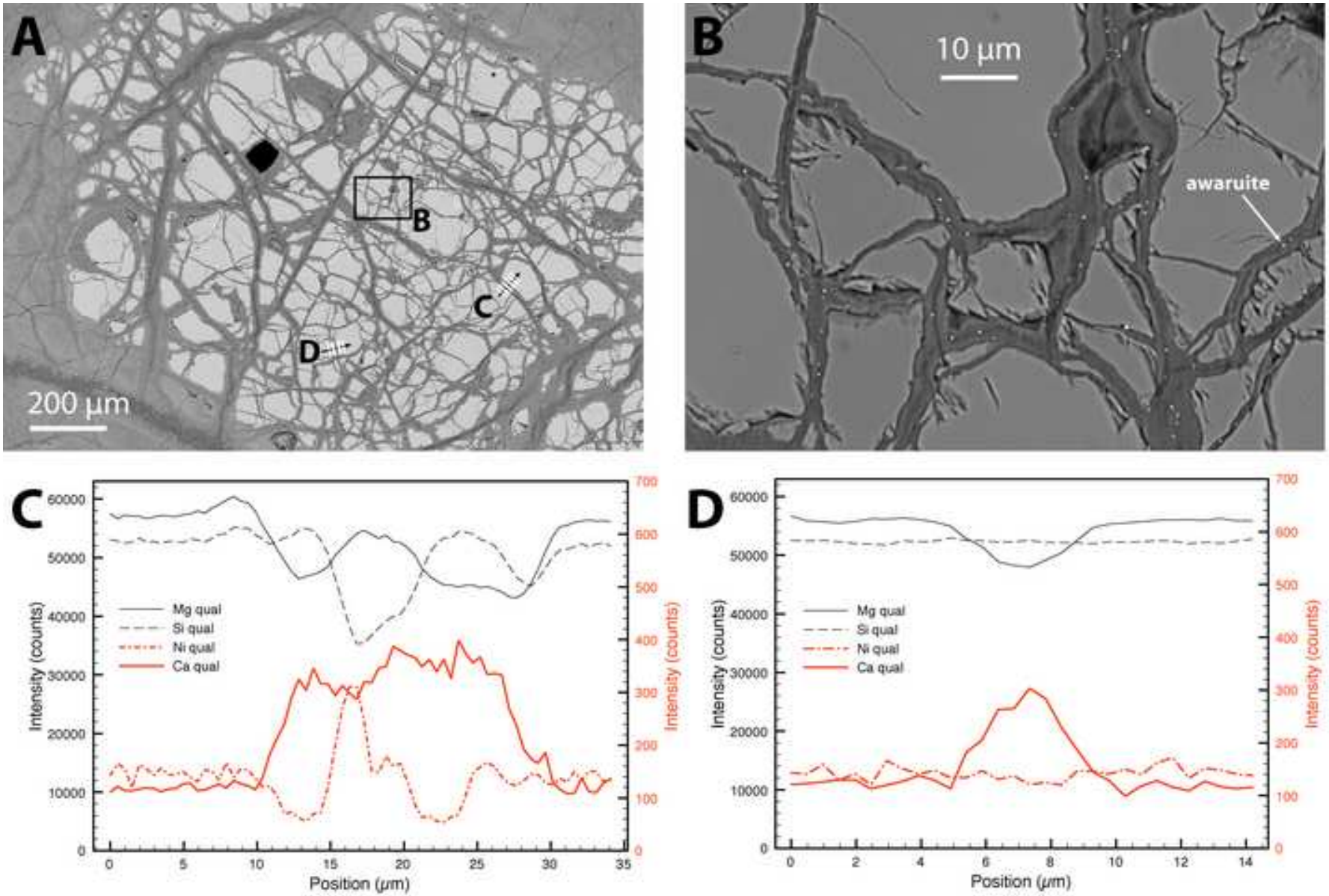

Figure4
Click here to download high resolution image

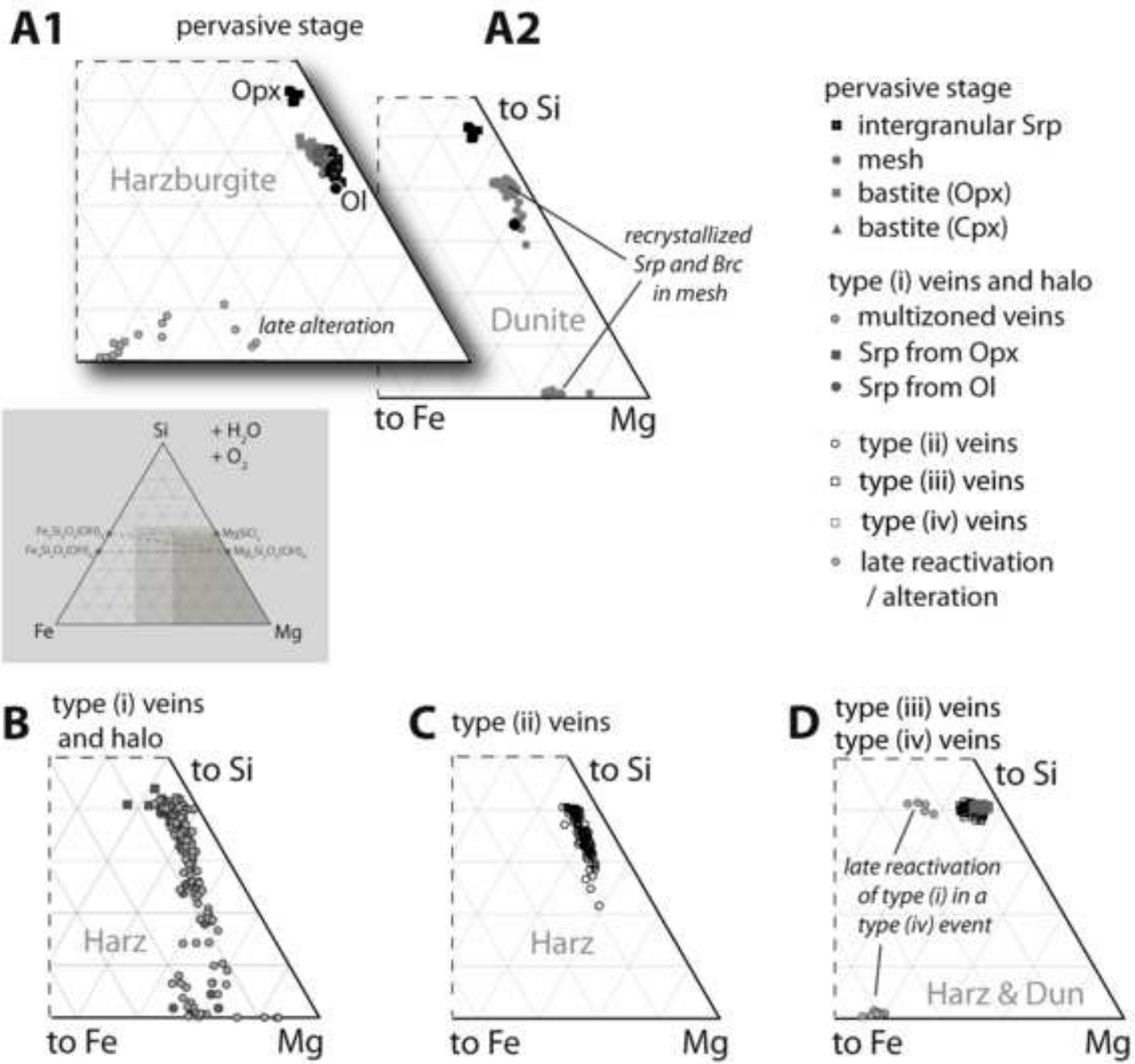

Figure5
Click here to download high resolution image

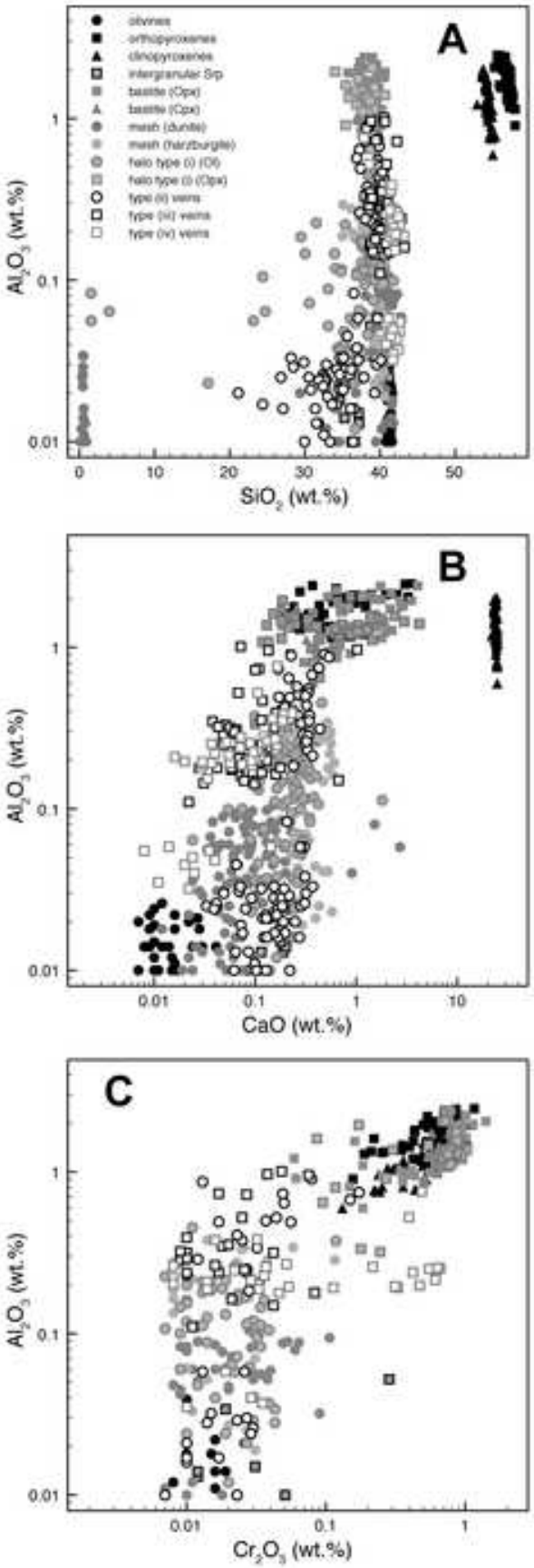

Figure6
Click here to download high resolution image

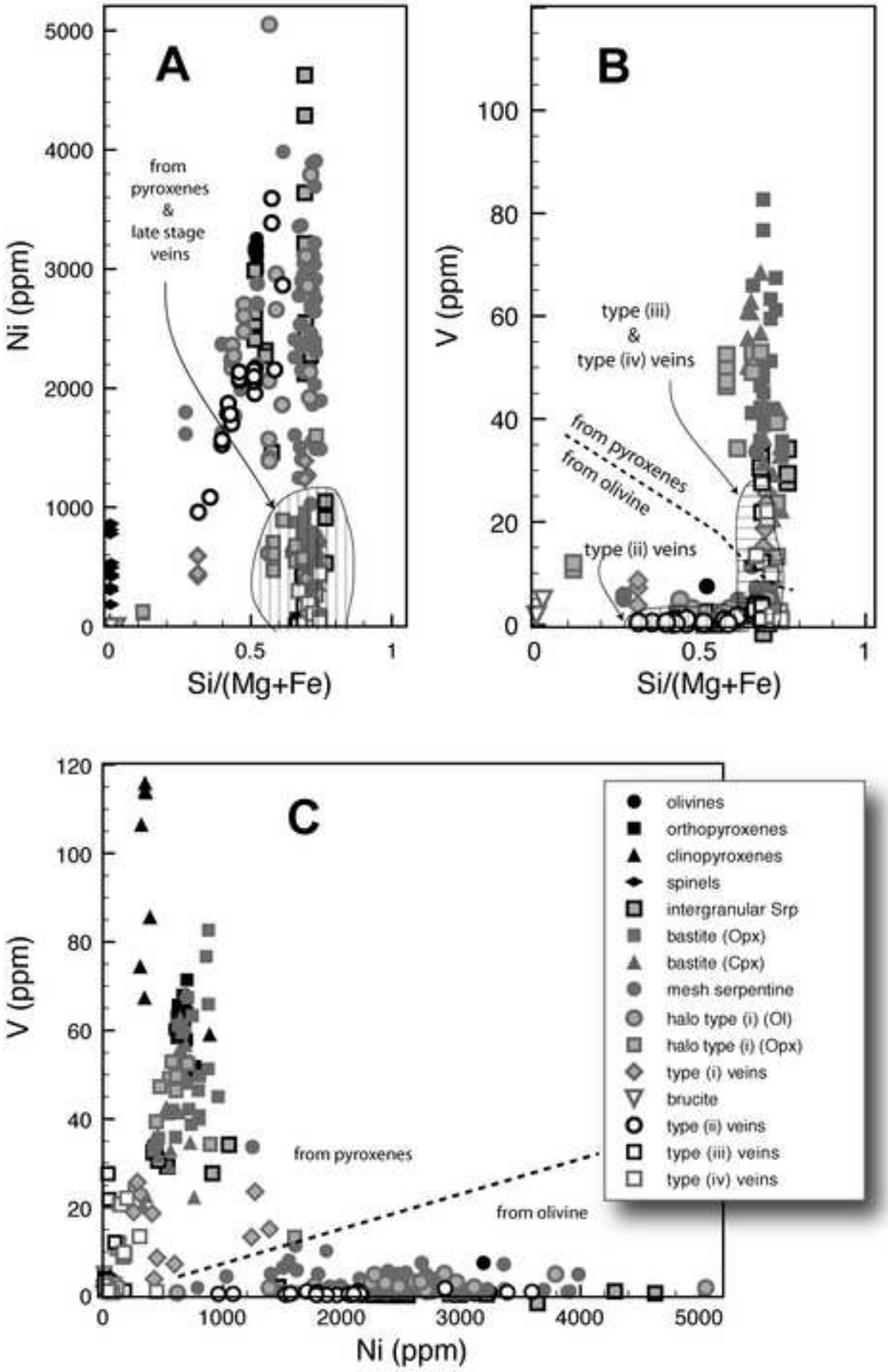

Figure7
Click here to download high resolution image

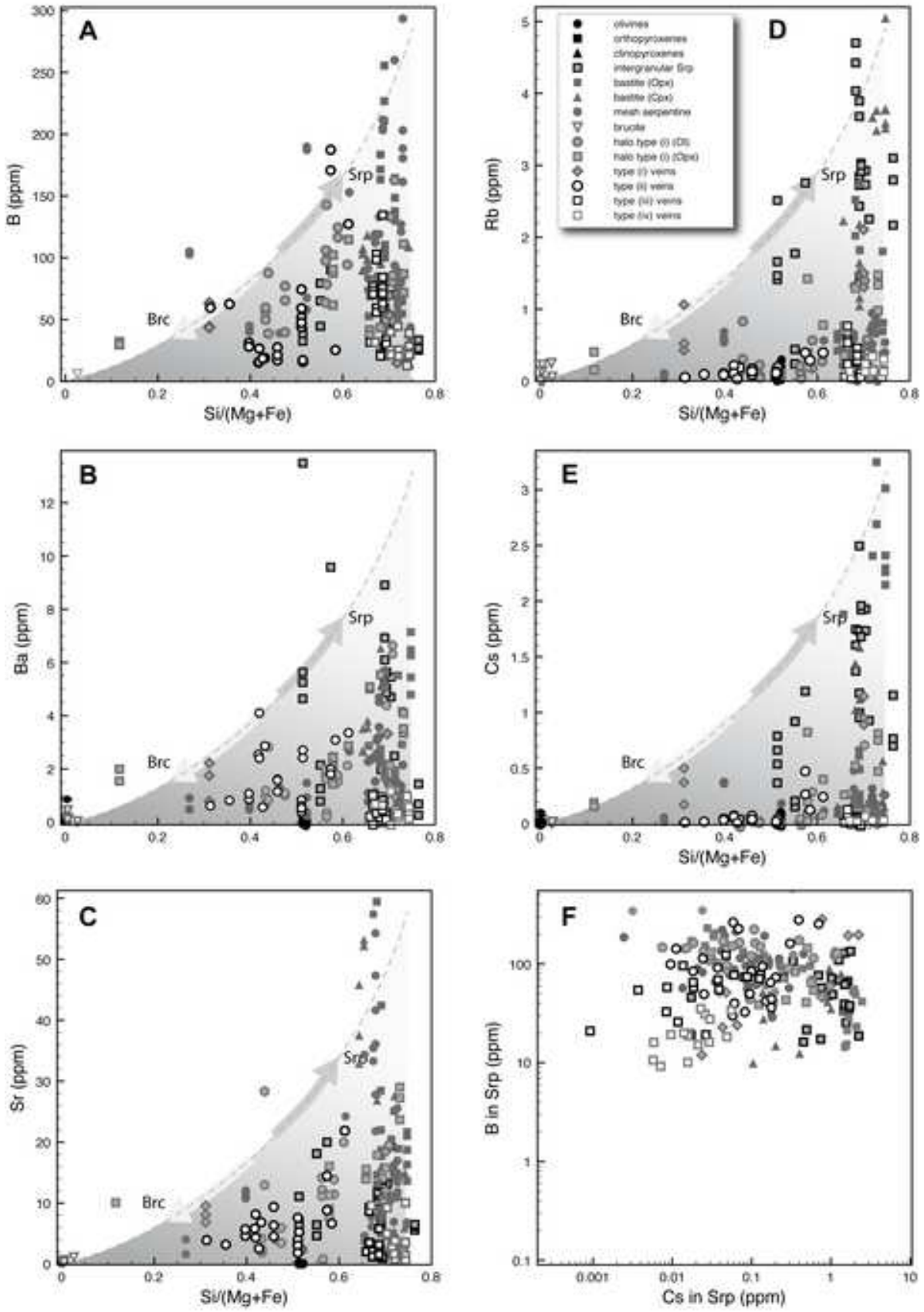

Figure8
Click here to download high resolution image

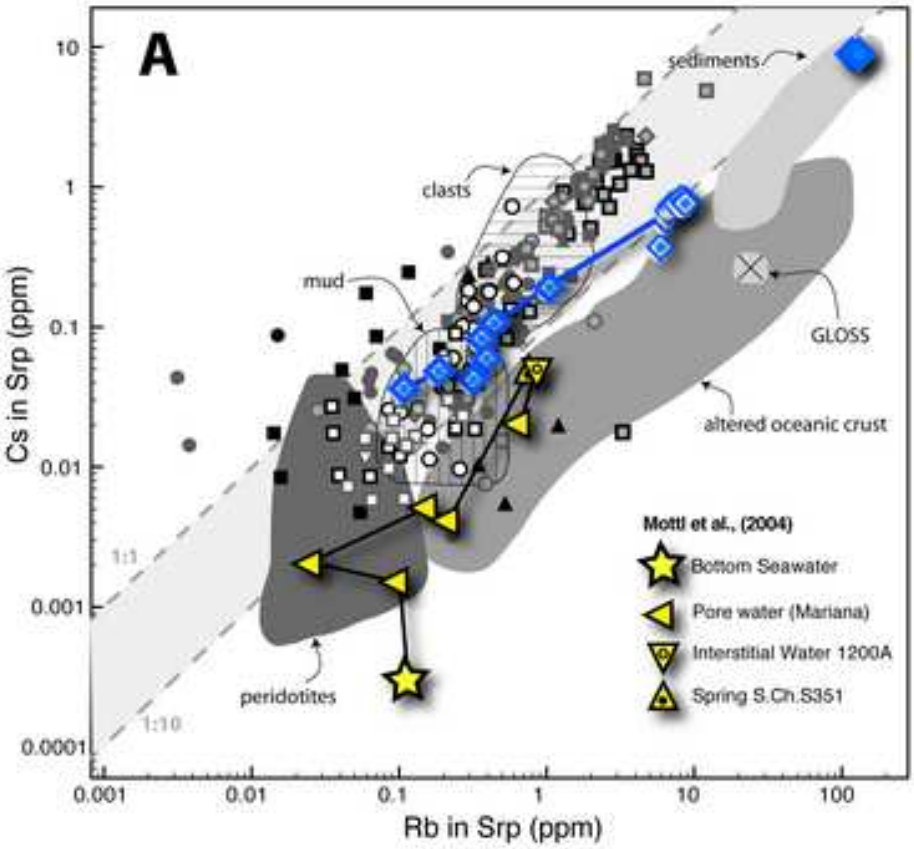

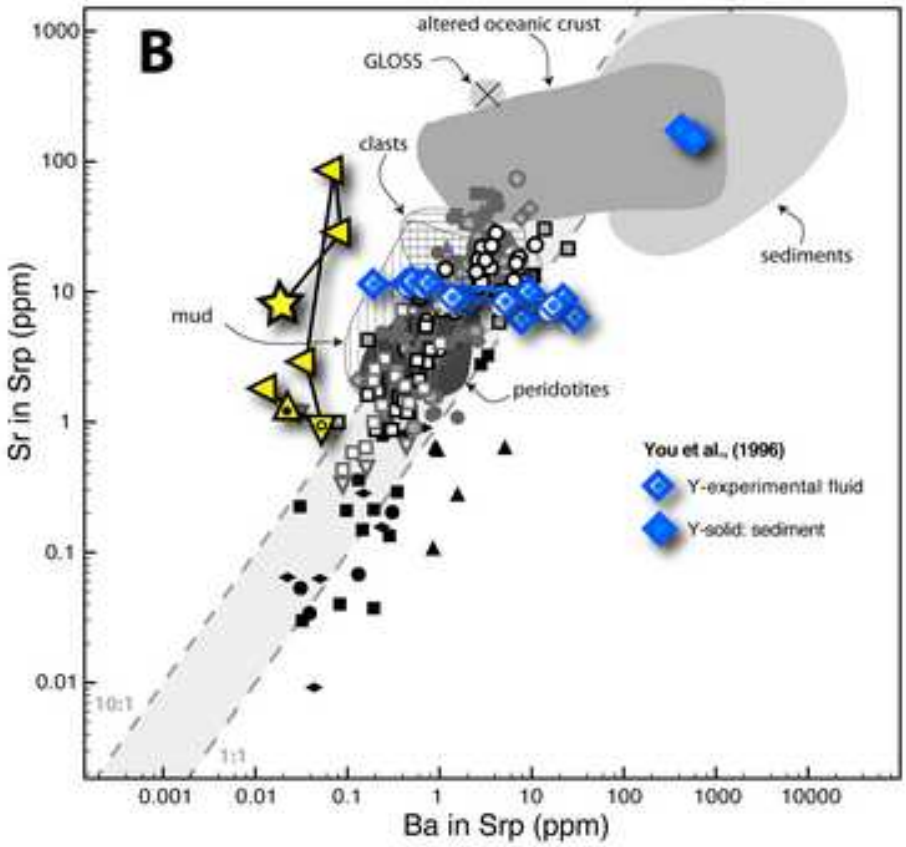

Figure9
Click here to download high resolution image

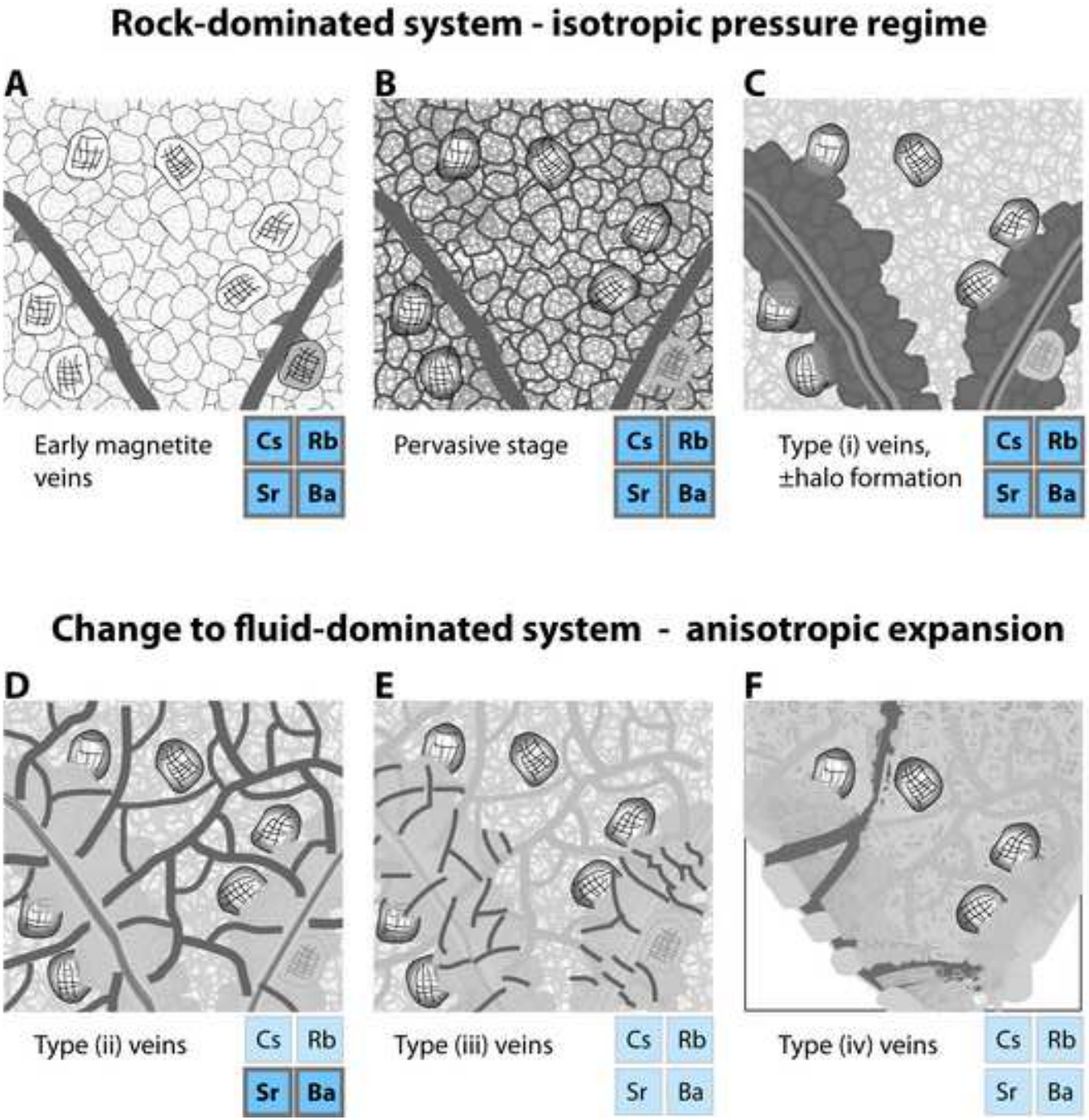

Table1
Click here to download Table: TABLE_1_Samples.pdf

Table 1. Samples (clasts) from South Chamorro Smt., Leg 195, Site 1200A.

Sample	Short hand	Subseafloor depth (mbsf)	Rock	% alteration
near rim				
1200A-3R-1_3-7	3R-1r	18.3	Dun	99
1200A-7R-2_40-43	7R-2r	52.1	Hz	65
1200A-9R-1_21-23	9R-1r	70.6	Dun	99
1200A-10R-1_25-27	10R-1r	80.2	Hz	95
1200A-11R-1_47-49	11R-1r	89.9	Hz	100
1200A-12R-1_8-10	12R-1r	99.1	Hz	100
1200A-13R-2_5-7	13R-2r	110.0	Hz	80
1200A-16R-1_52-54	16R-1r	138.1	Hz	98
1200A-16R-2_7-9	16R-2r	139.0	Hz	70
far from rim				
1200A-3R-1_15-17	3R-1c	18.35	Hz	99
1200A-7R-2_49-51	7R-2c	52.18	Hz	70
1200A-10R-1_25-27	10R-1c	80.15	hz	97
1200A-11R-1_49-50	11R-1c	89.89	Hz	70
1200A-12R-1_13-15	12R-1c	99.13	Hz	99
1200A-13R-2_15-17	13R-2c	110.1	Hz	85
1200A-16R-1_62-64	16R-1c	138.22	Hz	95
1200A-16R-2_11-12	16R-2c	139.06	Hz	75

Table2

Click here to download Table: TABLE_2_Representative_analyses_primary_minerals_1200A.pdf

Table 2. Representative electron microprobe analyses and in situ LA-ICP-MS data of relict primary minerals from Leg 195, Site 1200A, South Chamorro Smt.

Sample	7R-2	16R-2	16R-1	7R-2	13R-2	16R-1	7R-2	16R-1	9R-1	16R-2
Analys. no.	27-25	22-103	94-61	6-10	28-104	20-53	17-35	7-43	156-144	5-100
Mineral	Ol	Ol	Ol	Opx	Opx	Opx	Cpx	Cpx	Spl	Spl
rock type	*Hz*	*Hz*	*Hz*	*Hz*	*Hz*	*Hz*	*Hz*	*Hz*	*Dn*	*Hz*
wt.%										
SiO2	41.12	41.27	41.38	55.63	57.07	57.27	54.65	54.12	0.02	0.02
TiO2	0.00	0.00	0.00	0.00	0.02	0.02	0.00	0.03	0.03	0.01
Al2O3	0.01	0.00	0.02	2.47	1.50	1.31	1.18	1.18	5.97	24.79
Cr2O3	0.00	0.00	0.01	1.16	0.57	0.60	0.36	0.65	55.89	43.89
FeO	8.26	7.81	8.00	5.35	5.44	5.34	2.11	1.51	18.81	19.00
MnO	0.14	0.13	0.12	0.14	0.17	0.16	0.08	0.08	0.51	0.23
MgO	50.47	51.09	50.95	32.05	35.48	34.97	19.97	17.81	7.31	12.67
CaO	0.00	0.00	0.03	3.51	0.31	0.47	21.84	24.26	0.00	0.00
Na2O	0.00	0.00	0.00	0.00	0.01	0.02	0.00	0.05	0.00	0.00
K2O	0.00	0.00	0.00	0.00	0.00	0.00	0.00	0.01	0.00	0.00
Total	100.01	100.30	100.50	100.31	100.57	100.16	100.19	99.70	88.54	100.61
Oxygens	4	4	4	6	6	6	6	6	4	4
Si	1.00	1.00	1.00	1.93	1.95	1.97	1.97	1.97	0.00	0.00
Al	0.00	0.00	0.00	0.10	0.06	0.05	0.05	0.05	0.27	0.88
Ti	0.00	0.00	0.00	0.00	0.00	0.00	0.00	0.00	0.00	0.00
Cr	0.00	0.00	0.00	0.03	0.02	0.02	0.01	0.02	1.69	1.05
Fe3+*	n. c.	n. c.	n. c.	n. c.	n. c.	n. c.	n. c.	n. c.	0.03	0.06
Mg	1.83	1.84	1.83	1.66	1.81	1.79	1.07	0.97	0.42	0.57
Fe2+	0.17	0.16	0.16	0.16	0.16	0.15	0.06	0.05	0.57	0.42
Mn	0.00	0.00	0.00	0.00	0.00	0.00	0.00	0.00	0.02	0.01
Ca	0.00	0.00	0.00	0.13	0.01	0.02	0.84	0.94	0.00	0.00
Na	0.00	0.00	0.00	0.00	0.00	0.00	0.00	0.00	0.00	0.00
K	0.00	0.00	0.00	0.00	0.00	0.00	0.00	0.00	0.00	0.00
Sum	3.00	3.00	3.00	4.01	4.01	4.00	4.00	4.00	3.00	2.99
Mg/(Mg+Fe2+)	0.92	0.92	0.92	0.91	0.92	0.92	0.94	0.95		
Cr/(Cr+Al)									0.86	0.54
B [µg/g]	2.5	0.2	0.1	1.3	1.4	1.1	1.0	3.9	0.5	1.6
V [µg/g]	0.5	0.4	0.4	50.9	67.9	63.2	59.1	106.5	1002	763
Ni [µg/g]	3169	3030	2983	745	663	616	386	314	188	866
Rb [µg/g]	0.0	-0.1	0.3	0.0	0.1	0.1	0.5	0.3	n. d.	n. d.
Sr [µg/g]	0.2	0.0	0.2	0.2	0.2	0.2	5.1	1.6	0.0	0.2
Cs [µg/g]	0.0	0.0	0.0	0.0	0.0	0.1	0.3	0.2	0.0	0.0
Ba [µg/g]	0.0	0.1	-0.7	0.2	0.0	0.2	0.6	0.3	0.0	0.2

Note: Hz: Harzburgite; Dn: Dunite; * calculated assuming stoichiometry; n. d.: not determined; n. c.: not calculated; b. d. l.: below detection limit.

Table3

Click here to download Table: TABLE_3_Representative_analyses_serpentinization_products_1200A.pdf

Table 3. Representative electron microprobe analyses and in situ LA-ICP-MS data of serpentinization products from Leg 195, Site 1200A, South Chamorro Smt.

Sample	13R-2	13R-2	16R-2	16R-2	7R-2	7R-2	16R-2	16R-1	7R-2	16R-2	13R-2	3R-1	3R-1	9R-1
Analys. no.	72-126	77-128	245-132	239-63	261-50	280-49	74-83	153-37	66-40	210-125	44-114	#9-205	39-189	#8-174
Mineral	Srp	Srp-Brc	Srp	Brc	Srp-Brc	Srp-Brc	Srp	Srp-Brc	Srp-Brc	Srp	Srp	Srp	Srp	Srp
fabric type	type (i)	type (i)	type (i)-late	type (i)-late	halo (mesh)	halo (mesh)	halo (mesh)	halo (mesh)	halo (Opx)	halo (Opx)	halo (Opx)	Dn, mesh cnt.	Dn, mesh rim	Dn, recr. mesh
wt.%														
SiO2	40.86	21.24	41.45	0.51	36.42	34.87	40.04	27.47	34.04	38.08	40.87	40.16	40.73	41.00
TiO2	0.00	0.00	0.01	0.06	0.01	0.00	0.01	0.00	0.05	0.00	0.00	0.02	0.05	0.00
Al2O3	0.40	1.36	0.27	0.02	0.15	0.12	0.31	0.16	1.95	1.38	0.32	0.07	0.09	0.02
Cr2O3	0.13	0.04	0.00	0.02	0.02	0.00	0.00	0.03	0.17	0.81	0.00	0.02	0.00	0.00
FeO	5.52	8.82	5.08	42.00	5.83	6.65	4.29	6.99	6.36	6.36	4.07	3.94	4.46	2.85
MnO	0.11	0.19	0.09	0.94	0.16	0.11	0.09	0.15	0.09	0.11	0.08	0.10	0.12	0.07
MgO	37.97	41.31	38.13	32.58	38.55	39.31	38.23	39.33	37.28	34.95	37.98	37.67	38.05	39.80
CaO	0.22	0.30	0.09	0.02	0.16	0.24	0.36	0.41	0.19	0.72	0.37	0.07	0.08	0.03
Na2O	0.05	0.07	0.05	0.19	0.11	0.09	0.05	0.09	0.05	0.07	0.03	0.10	0.07	0.06
K2O	0.02	0.02	0.01	0.00	0.00	0.02	0.01	0.01	0.02	0.03	0.02	0.01	0.01	0.00
Total	85.34	73.91	85.19	76.37	81.56	81.61	83.49	74.81	81.15	82.65	83.89	82.28	83.78	83.88
Oxygens	7	7	7	2	7	7	7	7	7	7	7	7	7	7
Si	1.98	1.30	2.01	0.01	1.88	1.81	1.98	1.60	1.79	1.93	2.00	2.00	2.00	1.99
Al	0.02	0.10	0.02	0.00	0.01	0.01	0.02	0.01	0.12	0.08	0.02	0.00	0.00	0.00
Ti	0.00	0.00	0.00	0.00	0.00	0.00	0.00	0.00	0.00	0.00	0.00	0.00	0.00	0.00
Cr	0.00	0.00	0.00	0.00	0.00	0.00	0.00	0.00	0.01	0.03	0.00	0.00	0.00	0.00
Fe3+*	0.00	0.00	0.00	0.00	0.00	0.00	0.00	0.00	0.00	0.00	0.00	0.00	0.00	0.00
Mg	2.75	3.77	2.75	1.13	2.96	3.05	2.81	3.41	2.92	2.64	2.77	2.80	2.79	2.89
Fe2+	0.22	0.45	0.21	0.82	0.25	0.29	0.18	0.34	0.28	0.27	0.17	0.16	0.18	0.12
Mn	0.00	0.01	0.00	0.02	0.01	0.00	0.00	0.01	0.00	0.00	0.00	0.00	0.01	0.00
Ca	0.01	0.02	0.00	0.00	0.01	0.01	0.02	0.03	0.01	0.04	0.02	0.00	0.00	0.00
Na	0.00	0.01	0.00	0.01	0.01	0.01	0.01	0.01	0.01	0.01	0.00	0.01	0.01	0.01
K	0.00	0.00	0.00	0.00	0.00	0.00	0.00	0.00	0.00	0.00	0.00	0.00	0.00	0.00
Sum	5.01	5.66	4.99	1.99	5.12	5.19	5.02	5.40	5.15	5.01	4.99	5.00	5.00	5.01
Mg/(Mg+Fe2	0.92	0.89	0.93	0.58	0.92	0.91	0.94	0.91	0.91	0.91	0.94	0.94	0.94	0.96
B [µg/g]	69.51	44.15	14.98	n. d.	94.50	106.01	85.59	38.62	61.71	43.65	86.87	84.54	61.13	161.41
V [µg/g]	23.55	3.79	2.15	1.82	0.70	0.62	1.17	2.26	52.47	52.92	13.25	1.41	10.17	0.97
Ni [µg/g]	1269	422	1	2	1862	1571	2137	1766	704	573	1601	3038	1867	3908
Rb [µg/g]	2.11	1.06	0.16	0.14	0.27	0.21	0.58	0.31	0.35	1.29	1.48	0.92	0.73	0.00
Sr [µg/g]	18.41	8.06	3.97	0.64	19.96	14.17	19.50	12.97	7.77	17.90	29.02	13.44	4.22	2.04
Cs [µg/g]	1.14	0.50	0.03	n. d.	0.08	0.05	0.11	0.02	0.20	0.52	0.75	0.16	0.22	b. d. l.
Ba [µg/g]	1.40	1.75	1.23	0.45	2.13	1.61	6.64	0.84	1.44	5.54	3.51	1.09	0.65	0.61

Note: Hz: Harzburgite; Dn: Dunite; * calculated assuming stoichiometry; n. d.: not determined; n. c.: not calculated; b. d. l.: below detection limit.

Table 3. Repr

Sample	9R-1	9R-1	16R-2	16R-2	16R-1	7R-2	13R-2	16R-2	16R-1	7R-2	7R-2	16R-1	16R-2
Analys. no.	120-56	147-162	203-121	#24-111	137-23	#3-18	41-117	14-12	51-49	51-14	57-7	86-55	184-112
Mineral	Brc	Srp-Brc	Srp	Srp	Srp	Srp	Srp-Brc	Srp	Srp	Srp	Srp	Srp	Srp-Brc
fabric type	Dn, recr. mesh	Dn, mesh rim	Hz, mesh	Hz, mesh	Hz, mesh	gran. Ol	gran. Ol	gran. Ol	Bastite	Bastite	Bastite	Bastite (Cpx)	type (ii)
wt.%													
SiO2	0.47	34.11	40.26	39.94	39.21	39.96	35.89	39.98	39.29	40.59	38.38	38.42	36.17
TiO2	0.00	0.00	0.05	0.02	0.03	0.02	0.10	0.01	0.01	0.00	0.00	0.06	0.00
Al2O3	0.03	0.01	0.10	0.13	0.21	0.64	0.00	0.02	1.23	1.79	1.72	0.65	0.03
Cr2O3			0.00	0.02	0.01	0.11	0.03	0.00	0.56	0.90	0.94	0.30	0.01
FeO	16.12	6.74	4.90	6.00	6.61	5.35	5.61	3.38	6.44	7.69	5.92	5.38	5.85
MnO	0.33	0.09	0.10	0.12	0.12	0.11	0.09	0.04	0.14	0.22	0.17	0.11	0.07
MgO	54.40	41.85	38.50	36.08	36.43	36.48	41.16	40.46	33.36	31.93	33.51	36.60	40.40
CaO	0.03	0.09	0.25	0.36	0.23	0.35	0.16	0.22	1.93	2.90	2.17	0.43	0.18
Na2O	0.05	0.04	0.07	0.04	0.05	0.06	0.01	0.03	0.05	0.12	0.13	0.03	0.07
K2O	0.02	0.00	0.03	0.04	0.00	0.03	0.00	0.04	0.02	0.05	0.02	0.03	0.01
Total	71.95	82.99	84.31	82.90	83.03	83.35	83.47	84.27	83.19	86.31	83.16	82.16	82.85
Oxygens	2	7	7.00	7	7	7	7	7	7	7	7	7	7
Si	0.01	1.75	1.98	2.00	1.97	1.99	1.81	1.95	1.98	1.99	1.94	1.95	1.84
Al	0.00	0.00	0.01	0.01	0.01	0.04	0.00	0.00	0.07	0.10	0.10	0.04	0.00
Ti	0.00	0.00	0.00	0.00	0.00	0.00	0.00	0.00	0.00	0.00	0.00	0.00	0.00
Cr	0.00	0.00	0.00	0.00	0.00	0.00	0.00	0.00	0.02	0.03	0.04	0.01	0.00
Fe3+*	0.00	0.00	0.00	0.00	0.00	0.00	0.00	0.00	0.00	0.00	0.00	0.00	0.00
Mg	1.69	3.20	2.82	2.70	2.73	2.71	3.10	2.94	2.51	2.33	2.53	2.77	3.06
Fe2+	0.28	0.29	0.20	0.25	0.28	0.22	0.24	0.14	0.27	0.32	0.25	0.23	0.25
Mn	0.01	0.00	0.00	0.01	0.01	0.00	0.00	0.00	0.01	0.01	0.01	0.00	0.00
Ca	0.00	0.01	0.01	0.02	0.01	0.02	0.01	0.01	0.10	0.15	0.12	0.02	0.01
Na	0.00	0.00	0.01	0.00	0.00	0.01	0.00	0.00	0.00	0.01	0.01	0.00	0.01
K	0.00	0.00	0.00	0.00	0.00	0.00	0.00	0.00	0.00	0.00	0.00	0.00	0.00
Sum	1.99	5.25	5.02	4.99	5.02	4.99	5.18	5.05	4.97	4.95	5.00	5.03	5.17
Mg/(Mg+Fe2	0.86	0.92	0.93	0.91	0.91	0.92	0.93	0.96	0.90	0.88	0.91	0.92	0.92
B [µg/g]	n. d.	187.33	42.80	41.93	84.22	70.14	90.26	28.23	54.77	20.69	67.23	84.17	25.35
V [µg/g]	1.07	0.49	0.44	0.28	5.26	3.36	2.01	0.38	61.19	34.66	42.01	56.74	0.28
Ni [µg/g]	2431	2710	2458	2288	2534	2277	1462	2906	623	443	579	688	2154
Rb [µg/g]	0.23	0.13	3.00	2.93	0.54	2.25	2.76	2.85	3.76	3.51	3.66	2.52	0.29
Sr [µg/g]	0.32	2.34	13.77	10.81	35.43	19.32	19.99	7.68	14.36	13.62	25.09	26.85	6.66
Cs [µg/g]	n. d.	0.00	1.96	1.93	0.10	0.93	1.19	1.73	3.25	2.15	2.41	1.44	0.12
Ba [µg/g]	0.09	0.39	4.85	5.45	3.08	2.49	9.58	6.93	2.93	4.79	5.52	6.53	3.09

Note: Hz: Har

Table 3. Repr

Sample	16R-2	9R-1	7R-2	7R-2	13R-2	11R-1	16R-1	16R-1	16R-2	3R-1	3R-1
Analys. no.	185-122	#5-141	110-31	166-42	68-119	145-23	132-17	139-35	57-76	33-187	34-183
Mineral	Srp-Brc	Srp-Brc	Srp-Brc	Srp	Srp	Srp	Srp	Srp	Srp	Srp	Srp
fabric type	type (ii)	type (ii)	type (ii)	type (iii)	type (iii)	type (iii)	type (iv)	type (iv)	type (iv)	type (iv)	type (iv)
wt.%											
SiO2	28.47	33.46	30.72	40.14	40.48	41.28	42.15	41.29	42.46	40.82	41.12
TiO2	0.00	0.02	0.00	0.02	0.03	0.02	0.00	0.00	0.05	0.05	0.01
Al2O3	0.03	0.02	0.00	0.27	0.39	0.14	0.20	0.19	0.25	0.06	0.06
Cr2O3	0.02	0.00	0.00	0.00	0.01	0.01	0.05	0.00	0.55	0.00	0.00
FeO	7.26	6.19	6.86	5.37	8.70	5.92	5.32	5.64	4.51	3.73	4.75
MnO	0.14	0.13	0.12	0.13	0.15	0.10	0.09	0.10	0.09	0.10	0.11
MgO	43.10	42.66	42.95	38.25	35.75	38.36	38.77	38.09	38.61	38.97	38.08
CaO	0.22	0.06	0.19	0.07	0.16	0.04	0.03	0.09	0.08	0.04	0.14
Na2O	0.07	0.09	0.01	0.06	0.09	0.02	0.01	0.04	0.03	0.04	0.07
K2O	0.00	0.04	0.01	0.01	0.02	0.01	0.00	0.00	0.00	0.02	0.00
Total	79.37	82.66	81.01	84.39	85.86	85.92	86.65	85.48	86.65	83.89	84.48
Oxygens	7	7	7	7	7	7	7	7	7	7	7
Si	1.56	1.72	1.64	1.97	1.99	1.99	2.01	2.00	2.01	2.00	2.01
Al	0.00	0.00	0.00	0.02	0.02	0.01	0.01	0.01	0.01	0.00	0.00
Ti	0.00	0.00	0.00	0.00	0.00	0.00	0.00	0.00	0.00	0.00	0.00
Cr	0.00	0.00	0.00	0.00	0.00	0.00	0.00	0.00	0.02	0.00	0.00
Fe3+*	0.00	0.00	0.00	0.00	0.00	0.00	0.00	0.00	0.00	0.00	0.00
Mg	3.52	3.27	3.41	2.80	2.61	2.76	2.75	2.75	2.73	2.84	2.77
Fe2+	0.33	0.27	0.31	0.22	0.36	0.24	0.21	0.23	0.18	0.15	0.19
Mn	0.01	0.01	0.01	0.01	0.01	0.00	0.00	0.00	0.00	0.00	0.00
Ca	0.01	0.00	0.01	0.00	0.01	0.00	0.00	0.00	0.00	0.00	0.01
Na	0.01	0.01	0.00	0.01	0.01	0.00	0.00	0.00	0.00	0.00	0.01
K	0.00	0.00	0.00	0.00	0.00	0.00	0.00	0.00	0.00	0.00	0.00
Sum	5.44	5.28	5.37	5.02	5.01	5.01	4.99	5.00	4.97	5.00	4.99
Mg/(Mg+Fe2	0.91	0.92	0.92	0.93	0.88	0.92	0.93	0.92	0.94	0.95	0.93
B [μg/g]	16.06	43.96	27.53	134.62	73.16	29.20	23.84	39.95	14.69	25.36	44.66
V [μg/g]	0.21	0.47	0.27	21.83	3.03	1.17	9.30	22.08	2.62	0.95	1.79
Ni [μg/g]	1872	2151	2078	43	57	7	175	193	89	71	109
Rb [μg/g]	0.11	0.08	0.17	0.33	0.53	0.11	0.11	0.24	0.09	0.16	0.34
Sr [μg/g]	4.35	3.73	9.39	1.62	9.06	0.97	2.97	9.26	2.58	0.80	1.67
Cs [μg/g]	0.06	0.01	0.07	0.05	0.08	0.01	0.01	0.07	0.01	0.02	0.03
Ba [μg/g]	2.40	0.57	1.61	0.46	1.01	0.35	0.44	1.16	0.60	0.21	0.31

Note: Hz: Har

Table 4. Overview of selected properties of serpentine from different serpentinization events.

Serpentinization phase	Schematic fabric illustration	Secondary mineralogy	Serpentine geochemistry
Early magnetite veins	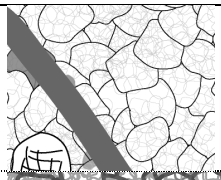	Srp, Mgt	n. a.
Pervasive stage	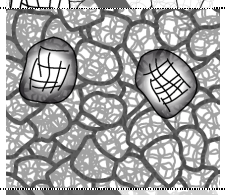	mesh: Lz* bastite: Lz*	mesh: < 0.5 wt.% Al_2O_3 in Srp; bastite: up to 2.4 wt.% Al_2O_3; Mesh: low V, high Ni; bastite: high V, low Ni; **Cs, Rb, Sr, Ba**
Type (i) veins	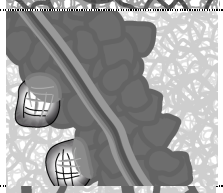	Liz*, Brc	up to 2.0 wt.% Al_2O_3; **Cs, Rb, Sr, Ba**
Type (ii) veins		Ctl*, Brc	up to 0.9 wt.% Al_2O_3; low V, high Ni; Cs, Rb, **Sr, Ba**
Type (iii) veins "*Frankenstein*"	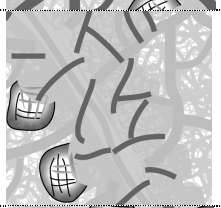	Ctl*	up to 1.0 wt.% Al_2O_3; V, low Ni; Cs, Rb, Sr, Ba
Type (iv) veins *multiple crack-seal*	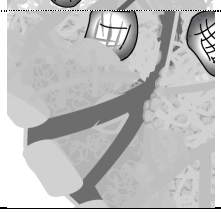	Ctl*	up to 0.8 wt.% Al_2O_3; V, low Ni; Cs, Rb, Sr, Ba

Note: n. a. not analyzed; *confirmed by micro-Raman; trace element contents: **bold**-relatively high values, plain-relatively low values.

Table5
Click here to download Table: TABLE_5_d18O_analysis.pdf

Table 5. Oxygen isotope data of serpentinization products from different serpentinization phases in ultramafic clasts from South Chamorro Smt., Leg 195, Site 1200A.

Sample	% serp	fabric type	minerals #	$\delta_{18}O$*
3R-1, 3-7 cm	100	type (iv) vein	Ctl	6.9
7R-2, 40-43 cm	97	halo region around type (i) vein	Liz, Ctl	7.6
10R-1_54-62 cm	100	vein, type (iv)	Ctl	6.4; 6.1
11R-1, 47-49 cm	100	vein in clast brown rim zone	Ctl	6.4
12R-1, 8-11 cm	100	bastite in brown clast rim zone	Ctl; Palyg, Sep, Sap (15 vol.%)	8.1
13R-2, 5-7 cm	100	chrysotile vein, type (iv)	Ctl	10.5
13R-2, 5-7 cm	100	serpentine, type (ii)		7.3
16R-2, 7-9 cm	97	type (ii) veins	Ctl, Liz, Brc (13 vol.%)	7.3
16R-2, 7-9 cm	97	type (i)/ reactivated by type (iv) vein	Liz, Ctl, Brc (4 vol.%)	6.6

Note: #determined by XRD; * VSMOW.